Spectral and temporal modulation and characterization of femtosecond ultra-short laser pulses

By

Gaelle Carine Mbanda Nsoungui

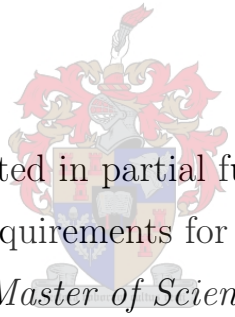

Thesis presented in partial fulfilment of the
academic requirements for the degree of
Master of Science
at Stellenbosch University

Supervisor: Prof. Erich.G. Rohwer
Co-Supervisor: Prof. Heinrich.PH. Schwoerer
Co-Supervisor: Dr. Pieter.H. Neethling

December 2012

Declaration

By submitting this thesis electronically, I declare that the entirety of the work contained therein is my own, original work, that I am the sole author thereof (save to the extent explicitly otherwise stated), that reproduction and publication thereof by Stellenbosch University will not infringe any third party rights and that I have not previously in its entirety or in part submitted it for obtaining any qualification.

December 2012

Abstract

Ultra-short laser pulses are useful in materials processing like melting and cutting metals, and medical applications such as surgery and many other fields. In this study, we characterize and control the temporal shape of the ultra-short pulses generated from a Ti:Sapphire femtosecond laser. It operates in the near infra-red spectral region, with a centre wavelength of 800 nm. The $4f$ pulse shaper is the main setup used to modulate spectral shape and characterize the laser pulse. The shaper consists of two diffraction gratings, two cylindrical lenses and a computer controlled liquid crystal spatial light modulator (LC-SLM). Gratings, lenses and LC-SLM are arranged in a $4f$ geometry, f being the focal length of the lenses. This setup is first analysed analytically and numerically using Fourier transform and the results obtained are then compared to those obtained from the experiment. The characterization of ultra-short pulses was done using three different autocorrelation techniques such as the intensity autocorrelation, the interferometric autocorrelation, and the pulse shaping autocorrelation which can act as interferometric autocorrelation when a nonlinear crystal β-barium borate (BBO) is placed exactly at the position of the experiment. These characterization techniques are based on the interaction between the laser pulse and a replica of it with a nonlinear crystal. The setups were implemented and measurements using the last two techniques were successfully conducted, with the pulse duration result in the range from 80-86 fs.

Opsomming

Ultrakort laserpulse het baie nut in verskeie velde waaronder materiaalprosessering (soos die smelt en sny van metale) en mediese toepassings (soos chirurgie) maar net twee voorbeelde is. In hierdie studie karakteriseer en beheer ons die vorm van ń ultrakort laserpuls, afkomstig vanaf ń Ti:Saffier femtosekonde laser, in tyd. Die laser straal in die naby-infrarooi spektrale gebied uit met ń sentrale golflengte van 800 nm. Ons gebruik ń sogenaamde 4f-pulsvormer om die spektrum van die laserpuls te moduleer en die laserpuls te karakteriseer. Die vormer bestaan uit twee diffraksieroosters, twee silindriese lense en ń rekenaarbeheerde vloeibare kristal ruimtelike-lig-modulator (LC-SLM). Die diffraksieroosters, lense en LC-SLM is in ń 4f-geometrie gerangskik, met f die brandpunt van die lense. Die opstelling is eers analities en numeries beskou deur van Fourier-transformasies gebruik te maak waarna die resultate wat verkry is met die van ń eksperiment vergelyk is. Die karakterisering van ultrakort laserpulse was met drie verskillende outokorrelasie tegnieke gedoen, naamlik ń intensiteits-outokorrelasie, ń interferometriese-outokorrelasie en ń pulsvormer-outokorrelasie. Die pulsvormer kan as ń interferometriese-outokorrelator optree indien ń nie-lineêre kristal β-bariumboraat (BBO) by die uitset van die pulsvormer geplaas word. Hierdie karakteriseringstegnieke is gebaseer op die interaksie tussen die oorspronklike laserpuls en ń kopie van die laserpuls in ń nie-lineêre kristal. Die nodige opstellings vir die metings is gemaak en die metings was suksesvol uitgevoer. Die pulslengte wat gemeet is, is in die orde van 80-86 fs.

Dedication

This thesis is dedicated to my parents, Albert.M. Kouala-landa and Léa.V. M. Guiri

Acknowledgements

God makes everything possible if you believe in him.

My sincere gratitude(s) are expressed to

• Prof. E.G. Rohwer. I am very grateful for his supervision and support throughout this project.
• Dr. P.H. Neethling for his wonderful supervision, guidance, patience, encouraging discussion and help on the experimental part of my work.
• Prof. H. Schwoerer for his encouragement and support that helped me to understand some dark spots on my work.
• Everyone who helped during the technical meetings.
• Dr. J. Mabiala for motivating me to undertake this study and for being there for me.
• Dr. G. Kuzamunu for his support.
• All my friends, especially Dirk, Farooq, Gibson, Peter, Wilfrid and Tchilabalo.
• Special thanks from my heart to my parents by the way they raised me since my childhood, the love, prayers, encouragements and supports to get where I am today. I love you so so much.

My studies were partially supported by the African Institute for Mathematical Sciences (AIMS) and the Faculty of Natural Sciences of the University of Stellenbosch.

Contents

List of Figures

List of Tables

Chapter 1

Introduction

The need for generating ultra-short laser pulses in the order of femtoseconds in duration has been of keen interest since the advent of the laser. Over the last 30 years, significant progress has been made on developing these ultra-short pulse lasers [29]. Indeed, the technological development of the present day gives access to subfemtosecond pulses with a pulsewidths as short as 0.65 fs [19]. These bursts of light are extremely short i.e., more than a million billion would fit within a second [17]. Nowadays, short pulses are used in several applications, including optical communication, biomedical optical imaging, high power laser amplification, etc [30].

Furthermore, the generation of these short pulses has contributed to the theory of light propagation in crystals [31]. Through recent advances, it has become possible to control the temporal shape of these femtosecond optical pulses using various pulse shaping techniques [14]. One such technique, using a $4f$-pulse shaper with a computer controlled spatial light modulator, will be studied in this work. One application of pulse shaping, namely autocorrelation, will be investigated [15].

1.1 Background

The $4f$-pulse shaper technique used to shape ultra-short pulses has developed rapidly. This technique relies on the development of a liquid crystal spatial light modulator (LC-SLM) with a large number of pixels. The inherently broad spectrum of ultrashort light

pulses (due to the wave property of the time-bandwidth product) is dispersed in space. At this position, the LC-SLM is able to alter the phase of the spectral components passing through each pixel [3]. In the last several years, pulse shaping has becomes a vital tool for coherent control of molecular dynamics and has produced results in many different research fields [33].

The $4f$ pulse shaper was introduced by Froehly [13] who performed his experiments on pulses in the order of 30 picoseconds, followed by Weiner who adapted the technique to pulses in the femtosecond regime [29]. Initially, the technique was limited only to the manipulation of either the phase or the amplitude of the different spectral components in the pulse. However, with the advancement in technology and research in the field, complete control over both phase and amplitude and hence the vectorial nature of the pulse, is now possible [15]. Therefore, the Fourier transform of the optical pulse can be performed in a real experiment. The $4f$ pulse shaper used in this work is represented as:

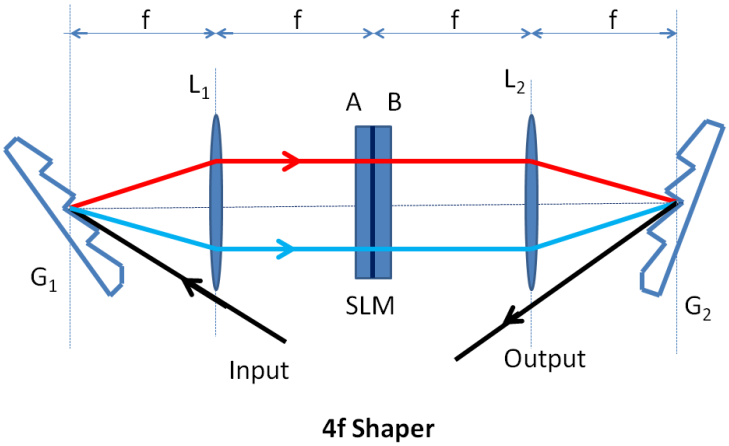

FIG. 1.1. $4f$ geometry.

It contains two holographic gratings, two cylindrical lenses and a Spatial Light Modulator (SLM) at a focal plane. Each element is placed at a distance equal to the focal length f. The $4f$ geometry will be analysed in subsection 2.6.1.

1.2 Motivation for this study

The motivation of the theoretical part of this work is to compile a detailed theory of a Spatial Light Modulator (SLM) implemented in a $4f$-geometry. This is done modelling the setup using Fourier optics.

The main motivation of the experimental part in this thesis is to control and characterise temporal short pulses using a spatial light modulator in a $4f$-geometry. As an example of this control, the $4f$-pulse shaper was used to perform an autocorrelation measurement. This measurement was compared to typical measurements using a background free autocorrelator and an interferometric autocorrelator [15].

Chapter 2

Theory

This work focuses on understanding the $4f$-pulse shaper and the characterization of ultra short pulses. The theoretical background concerning this study is introduced in this chapter. In section 2.1, the concept of light propagation through an anisotropic material is described. Section 2.2 introduces the phenomenon of light polarization and its characterization. Section 2.3 discusses how the amplitude and/or phase of polarized light can be modulated using the SLM in a $4f$-pulse shaper setup. The concept of nonlinear effects is described in section 2.4. Two examples for temporal pulses were investigated using Fourier transforms in section 2.5. The modeling of the $4f$-pulse shaper under specific conditions is presented in section 2.6.

2.1 Light propagation through an anisotropic medium

All experiments in optics are based on the propagation of light which is an electromagnetic wave, with electric and magnetic components, **E** and **H** [25]. **E** and **H** are orthogonal with respect to the propagation direction and each other [2]. The orientation of the oscillation of the electric field **E** defines the polarization of the light.

The polarization of light is of special importance when one considers light propagating through a transparent material. The direction of polarization with regards to the optical axis of the material determines the refractive index that is experienced by the light. For optically isotropic materials this is of no consequence as there is no defined optical axis.

For optically anisotropic materials this is very important, as the orientation of the polarization with respect to the optical axis determines the refractive indices that the light will experience. To explain this better, we need to introduce the concept of birefringence. We will consider a plane wave travelling through an uniaxial crystal. The plane wave with wave vector k and frequency ω travelling in the z-direction can be described as

$$\mathbf{E} = \mathbf{E}_0 \exp\left[-i(kz - \omega t)\right], \tag{2.1}$$

where $\mathbf{E}_0$ is the amplitude of the electric field.

2.1.1 Birefringence

A material is said to be birefringent if it has a well defined optical axis, and two distinct refractive indices dependent on the orientation of the incident light polarization with respect to this optical axis. (Light polarization will be discussed in detail in section 2.2). If the polarization of the light is parallel to the optical axis, it experiences an index of refraction, n_e, and is known as the extraordinary ray, whilst light polarized perpendicular to the optical axis experiences an index of refraction, n_0, and is known as the ordinary ray. This implies that the two perpendicular components of arbitrarily polarized light propagating through a birefringent medium will experience different indices of refraction and propagate at different velocities through the medium. The result is that the two components will have a distinct phase shift with respect to each other, dependent on the difference of the two refractive indices and here the path length through the material.

If we now consider a beam of randomly polarized light propagating in the z-direction entering a birefringent material, we can write the beam in its two orthogonal components with respect to the optical axis of the material [18]:

$$\mathbf{E}_x = \mathbf{i} E_{0x} \cos(k_x z - \omega t), \tag{2.2}$$

$$\mathbf{E}_y = \mathbf{j} E_{0y} \cos(k_y z - \omega t), \tag{2.3}$$

where ω is the angular frequency, $\mathbf{i}$ and $\mathbf{j}$ are the unit vectors and k_x and k_y are the wave vectors of the two components. Since the medium is birefringent, the two components experience different refractive indices and hence a relative phase shift. This phase shift

can be calculated by considering the total phase of each of the two components, namely $\phi_x = k_x z - \omega t$ and $\phi_y = k_y z - \omega t$ and calculating the difference. If one assumes that $\mathbf{E}_x$ is the extraordinary ray and $\mathbf{E}_y$ is the ordinary ray, then the phase difference becomes

$$\begin{aligned} \phi &= \phi_x - \phi_y && (2.4)\\ &= k_x z - k_y z && (2.5)\\ &= \frac{z\omega n_e}{c} - \frac{z\omega n_0}{c} && (2.6)\\ &= \frac{\ell\omega}{c}(n_e - n_0) && (2.7) \end{aligned}$$

with ℓ the length of the birefringent material and c the speed of light in vacuum.

2.2 Light polarization

The polarization of light refers to the plane in which the electric field of the electromagnetic wave oscillates [2]. In general, light can be arbitrarily polarized, having electric field oscillations in many different planes with all these oscillations having different phase relations with respect to each other. All these different oscillations can always be de-convoluted into two orthogonal components which can then be combined through vector addition.

$$\mathbf{E} = \mathbf{i}E_{0x}\cos(kz - \omega t) + \mathbf{j}E_{0y}\cos(kz - \omega t + \phi), \tag{2.8}$$

In this section we will focus on two specific cases namely linear polarization and circular polarization.

2.2.1 Linear polarization

In Equation (2.8), let us consider a phase difference between the two orthogonal components such that $\phi = 2n\pi$ for an integer n. This has the result that both components travel perfectly in phase with resultant amplitude equal to $(\mathbf{i}E_{0x} + \mathbf{j}E_{0y})$, obtained from Equation (2.8). The orientation of the oscillations of the resultant wave is fixed in a plane and does

not vary as the beam propagates. Let us now consider the case where $\phi = (2n+1)\pi$ for an integer n. This refers to electric field components that are exactly 180° out of phase. The resultant is still a linearly polarized beam, just rotated by 90° from the previous case. The condition for linearly polarized light can thus be summarized as follows: if the phase difference between any two orthogonal components of the electromagnetic wave is an integer multiple of π, the resultant beam is linearly polarized.

2.2.2 Circular polarization

Circular polarization refers to the case where the phase shift between the two orthogonal components described in Equation (2.8) is exactly $\pm\frac{\pi}{2}$. This results in the vector sum of the two components rotating about the propagation axis with a constant scalar amplitude, ($E_{0x} = E_{0y} = constant$). More generally, the values of phase shift are $\phi = \mp\frac{\pi}{2} + 2\pi m$ for an integer $m = 0, \pm1, \pm2, \ldots$. Considering $m = 0$ and $\phi = -\frac{\pi}{2}$ and applying trigonometric transformation, Equation (2.8) becomes

$$\mathbf{E} = E_0 \left(\mathbf{i}\cos(kz - \omega t) + \mathbf{j}\sin(kz - \omega t)\right). \tag{2.9}$$

Both components are positive and the direction of the resultant field varies with time and rotates in clockwise direction around the propagation axis as the beam travels. This is known as right circularly polarized light. For $\phi = +\frac{\pi}{2}$, Equation (2.8) becomes

$$\mathbf{E} = E_0 \left(\mathbf{i}\cos(kz - \omega t) - \mathbf{j}\sin(kz - \omega t)\right). \tag{2.10}$$

This represents a resultant field that rotates counterclockwise with respect to the propagation axis. This is known as left circularly polarized light. For phase shift $0 < \phi < \frac{\pi}{2}$ and $\frac{\pi}{2} < \phi < \pi$ we end up with cylindrically polarized light. Linear and circularly polarized light can be considered special cases of the more general case of elliptically polarized light.

2.2.3 Jones matrix

The 2×1 Jones vectors are convenient ways of describing the polarization of a laser beam, whilst the 2×2 Jones matrices represent a convenient way to describe the influence of

a polarizing optical element on the said polarization vector. The general format of an electromagnetic plane wave is given by [25]:

$$\mathbf{E}_i = \mathbf{i}E_{0x}e^{-i(k_x z-\omega t)} + \mathbf{j}E_{0y}e^{-i(k_y z-\omega t-\phi)} \ , \tag{2.11}$$

This can be rewritten as the following vector (Jones vector):

$$E_i = \begin{bmatrix} |E_{ix}| \\ |E_{iy}| \end{bmatrix} = \begin{bmatrix} |E_{0x}|e^{-i(k_x z-\omega t)} \\ |E_{0y}|e^{-i(k_y z-\omega t-\phi)} \end{bmatrix}$$

where the fields $E_{ix} = E_{0x}\exp(-i(k_x z - \omega t))$ and $E_{iy} = E_{0y}\exp(-i(k_y z - \omega t - \phi))$ are scalar complex components containing the phase and amplitude information. This vector is a general form for one wave that describes the polarization with all the information of the defined wave.

A number of examples of representing polarizing optics as Jones matrices and their corresponding influence on an input electromagnetic wave is presented in the next couple of subsections. In principle, however, the influence of the specific polarizing element can be calculated by multiplying the incident beam (Jones vector) with the appropriate Jones matrix (J). The polarization state after the specific optical element, E_t, is obtained in this fashion

$$E_t = JE_i \, . \tag{2.12}$$

In general, when light propagates through various optical elements, this Equation is not a commutative matrix series of the respective J-matrices. The final resultant field is then calculated in normal order of elements as follows:

$$E_t = J_n \ldots J_2 J_1 E_i, \tag{2.13}$$

where n is the number of the optical elements contained in the system.

2.2.4 Linear polarizer

A linear polarizer is an optical device used to transmit only one polarization direction and block all the others. The polarizer transmits the polarization parallel to its polarization axis. A linear polarizer, aligned with the x-axis, can be represented by the following Jones

matrix

$$P_x = \begin{bmatrix} 1 & 0 \\ 0 & 0 \end{bmatrix}$$

It would let a light beam polarized along the x-axis pass completely. This can be seen by considering the product of the above mentioned Jones matrix and the vector describing a polarized beam along the x-axis, p_x.

$$p_x = \begin{bmatrix} 1 \\ 0 \end{bmatrix}$$

The product $P = P_x p_x$ can be expressed as:

$$P = \begin{bmatrix} 1 & 0 \\ 0 & 0 \end{bmatrix} \begin{bmatrix} 1 \\ 0 \end{bmatrix} = \begin{bmatrix} 1 \\ 0 \end{bmatrix}$$

A beam polarized along the y-direction would be completely blocked since it has no component along the x-direction. Any beam polarized somewhere between x and y would have only the electric field component parallel to the x-axis pass. Since this component depends on the cosine of the angle between the polarization and the x-axis, a relationship between the transmitted electric field and the polarization angle can be obtained. Since it is typical to measure the intensity and not the electric field in most experiments, this relationship is most often expressed in terms of the irradiance which is proportional to the square of the electric field

$$I(\theta) = \frac{c\varepsilon_0}{2} E_0^2 \cos^2(\theta) = I(0) \cos^2(\theta), \tag{2.14}$$

with $I(0) = \frac{c\varepsilon_0}{2} E_0^2$ the irradiance incident on the polarizer, ε_0 the permittivity of free space, c the speed of light in vacuum and θ the angle between the polarization of the beam and the polarization axis of the polarizer. This Equation is known as Malus's Law introduced in 1809 by Etienne Malus [18]. Equation (2.14) is plotted in FIG. 2.1, for the range $-90°$ to $90°$.

2.2.4.1 Wave plates

A wave plate in general operates by shifting the relative phase between the two orthogonal polarization components of the beam that passes through the wave plate. It consists of a

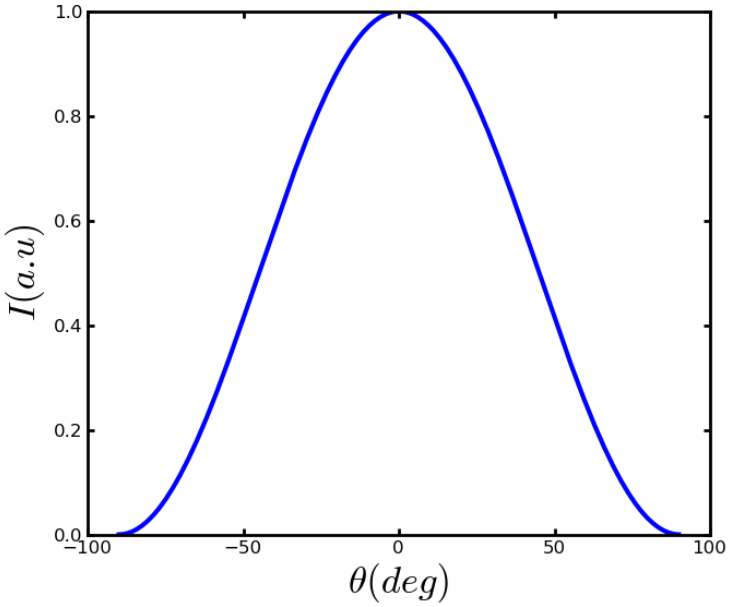

FIG. 2.1. Malus's law for $-90° < \theta < 90°$.

birefringent material with a defined orientation and thickness. The crystal is cut in such a fashion that its optical axis is parallel to the surface of the plate. This means that light polarized along this axis travels at a different speed than the light component perpendicular to this axis. In general we distinguish between two different types of wave plates, quarter- and half-wave plates, dependent on the relative phase shift that the wave plate induces.

Half-wave plate

In the case of a half-wave plate, the one polarization component is retarded by half a wavelength or 180°. This has the result of changing the polarization direction of linearly polarized light. The Jones matrix representation of a half-wave plate H_x with its optical axis along the x-axis is given by:

$$H_x = \begin{bmatrix} 1 & 0 \\ 0 & -1 \end{bmatrix}.$$

If linear polarized light, with polarization direction 45° with respect to the x-axis, is incident on the half-wave plate the half-wave plate will rotate the polarization by 90°. Light

polarized at 45° degrees with respect to the x-axis is given by

$$h_i = \frac{1}{\sqrt{2}} \begin{bmatrix} 1 \\ 1 \end{bmatrix}.$$

If this field is now multiplied by the Jones matrix, H_x, the resultant field is given by h_f,

$$h_f = \frac{1}{\sqrt{2}} \begin{bmatrix} 1 & 0 \\ 0 & -1 \end{bmatrix} \begin{bmatrix} 1 \\ 1 \end{bmatrix} = \frac{1}{\sqrt{2}} \begin{bmatrix} 1 \\ -1 \end{bmatrix}.$$

The incident beam was normalized. It can therefore clearly be seen that the half-wave plate only changed the polarization direction and not the beam amplitude and energy was conserved.

Quarter-wave plate

Quarter-wave plates operate in a similar fashion as half-wave plates, except that they introduce a quarter of a wavelength, or 90°, phase shift between the two orthogonal components of the incident polarized light [12]. This has the result that a quarter-wave plate can be used to convert linearly polarized light to circularly polarized light and vice versa [32].

The Jones matrix representation for a quarter-wave plate aligned along the x-axis is given by

$$Q_x = \begin{bmatrix} 1 & 0 \\ 0 & i \end{bmatrix}.$$

The effect of a quarter-wave plate can again be seen if we consider a beam, linearly polarized at 45° with respect to the x-axis, incident on the quarter-wave plate described by Q_x. Such a beam will again look like the beam described by h_i.

$$h_i = \frac{1}{\sqrt{2}} \begin{bmatrix} 1 \\ 1 \end{bmatrix}.$$

The product between Q_x and h_i is then given by h_t

$$h_t = \frac{1}{\sqrt{2}} \begin{bmatrix} 1 & 0 \\ 0 & i \end{bmatrix} \begin{bmatrix} 1 \\ 1 \end{bmatrix} = \frac{1}{\sqrt{2}} \begin{bmatrix} 1 \\ i \end{bmatrix}.$$

This results in left circularly polarized light. Again, since the incident beam was normalized, it can be seen that the quarter-wave plate only changed the polarization and not the amplitude of the incident beam. Energy was thus again conserved.

If the incident beam was not polarized at 45° with respect to the optical axis of the quarter-wave plate i.e., at some angles between 0° and 45°, the polarization of the resultant field would be varying in degrees and in amplitude. This leads to an elliptically polarized light.

2.3 Spatial light modulator (SLM)

The spatial light modulator (SLM) used in this study can be thought of as an array of 640 individual light modulators (pixels). Each pixel consists of two back-to-back liquid crystal (LC) cells which can independently change the phase of the light passing through the pixel [1]. When such an SLM is used in a $4f$-geometry, it is possible to shape an incident laser pulse in time [23, 28]. Shaping a laser pulse in time has many applications, pump probe spectroscopy and short pulse characterization being two such applications.

2.3.1 Liquid crystal (LC)

Liquid crystals (LCs) are interesting materials from a physics point of view since their properties lie somewhere between solids and liquids. They are used in optical image processing and in diffractive optics [22]. To simplify matters, LCs are often modeled as ellipsoids. The way in which these LCs are arranged next to each other with different geometrical configurations defines different types of liquid crystals. Under the influence of mechanical or electrical forces, adjacent molecules can rotate or slide with respect to one another, thus exhibiting some of the properties of a liquid. However, constraints on the geometrical arrangement of the collection of molecules introduce some properties related to those of solids. The type of LCs of interest in our work is nematic liquid crystals (NLCs). The individual LCs within the entire volume of the material favour parallel orientation and their respective centres are randomly located. An illustration of this type of liquid crystal is given in FIG. 2.2.

Each cell of the SLM contains a thin layer of NLCs sandwiched between 2 parallel glass

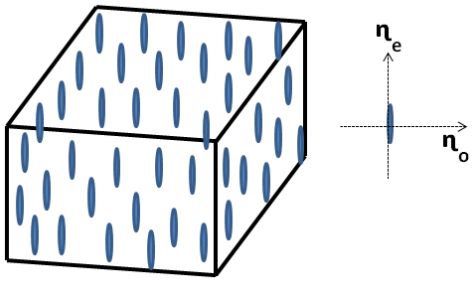

FIG. 2.2. An illustration of an arrangement of nematic liquid crystals.

plates. On the inside of the glass plate (side facing the NLC's) there is first a thin patterned transparent conductive ITO (Indium Tin Oxide) electrode which is again covered by an alignment layer which is responsible for the geometric orientation of the NLC molecules. The alignment layer leads to the NLCs being homogeneously orientated in a known direction [1]. These NLCs are initially parallel to the glass plates when there is no electric field present. Note that the optical behaviour of liquid crystals can be compared to that of uniaxial birefringent crystals.

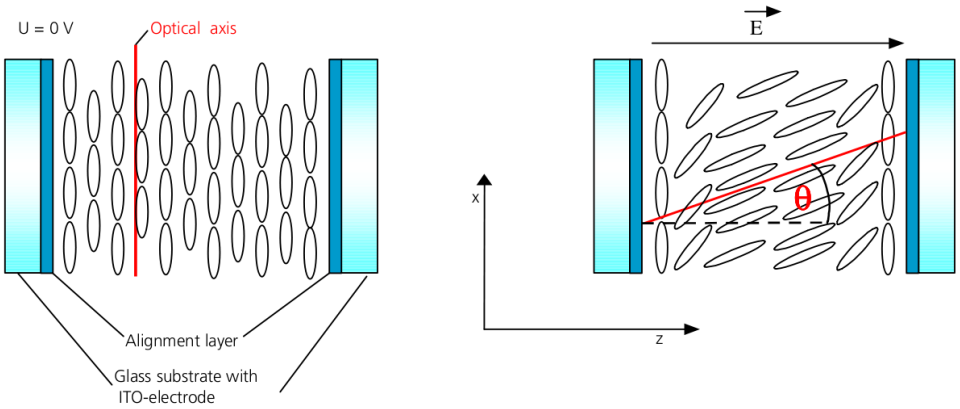

FIG. 2.3. Orientation of the liquid crystal molecules in the SLM cell without and with an electric field being applied [1].

The first figure on the left in FIG. 2.3 illustrates the orientation of the NLCs within a cell without an applied voltage, whilst the figure in the right shows the NLC molecules tilted such that the optical axis forms an angle θ with the propagation axis (z-axis) due to the applied electric field. The field enters the cell perpendicularly. If the direction of

an electromagnetic field is polarized along the x-axis, then in the case of no electric field applied to the NLC, no birefringence will occur since the polarization is parallel to the optical axis. However, when a voltage is applied across the cell, the polarization is no longer parallel to the optical axis and the beam will experience birefringence. The incident field will split into two perpendicular components with a refractive index difference. One is extraordinary, which is a function of the angle θ on x-axis and the second is ordinary on y-axis, which decreases continuously as the applied voltage increases. Thus, we can write the induced phase difference between the two components (Equation (2.7)) as a function of the applied voltage

$$\phi(U) = \frac{\omega l}{c} \left[n_\theta(U) - n_0 \right], \tag{2.15}$$

In terms of the specific phases of the extraordinary and ordinary waves, we can write the induced phase change as [1]

$$\phi(\omega, U) = \Delta\phi = \phi_e - \phi_o = \frac{\omega l}{c} \Delta n(\omega, U). \tag{2.16}$$

where U is the applied voltage and $n_\theta(U)$ is given by [1]

$$\frac{1}{n_\theta^2(\omega, U)} = \frac{\cos^2\theta(U)}{n_o^2(\omega)} + \frac{\sin^2\theta(U)}{n_e^2(\omega)}.$$

The phase retardation contains a constant phase and a voltage dependent phase. For high propagating voltages, the phase retardation vanishes when the constant phase is always constant. The maximum phase value $\phi(\omega, U)$ is obtained at $U = 0$.

The SLM used in this work consists of two separately controllable LC displays acting on phase and amplitude independently but simultaneously. Each mask contains 640 pixels, which can be considered to be individual light modulators, with a uniform width of 97 μm, separated from one another by a spacing of 3 μm. The total length of each display is 64 mm. FIG. 2.4 illustrates the way these displays are orientated with respect to each other. It also shows the polarizer which needs to be placed behind the SLM in order to perform amplitude modulation

The displays are positioned back to back and orientated such that the alignment layers

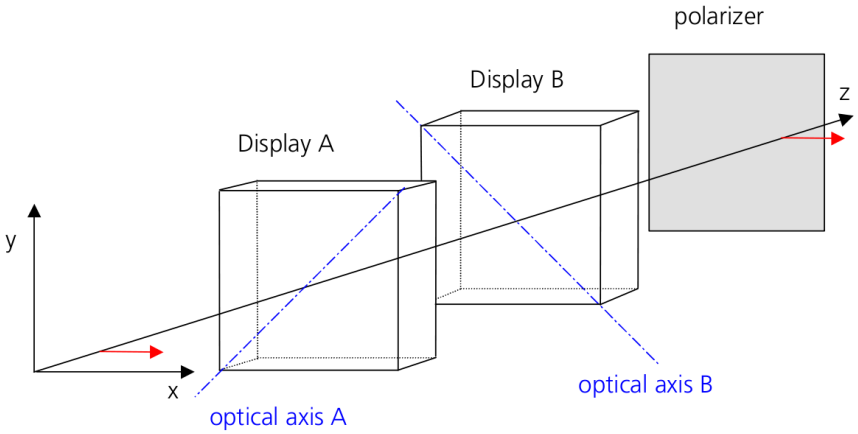

FIG. 2.4. The figure shows the relative orientation of the two NLC displays in the SLM and the position of the polarizer which is necessary for amplitude modulation [1].

are perpendicular with respect to each other. The direction of incident light is polarized at 45° with respect to the alignment direction of both displays. The most convenient way to describe the effect of the two SLM displays and the polarizer on the incident wave is with the help of Jones matrices. The output field is the product of the matrices of the two SLM displays, the polarizer and the linearly polarized incoming beam E_i. Each display introduces a phase shift, $\Delta\phi_1$ and $\Delta\phi_2$. The output field, E_t, can then be described as

$$E_t = \begin{bmatrix} 1 & 0 \\ 0 & 0 \end{bmatrix} \begin{bmatrix} \cos(\frac{\pi}{4}) & \sin(\frac{\pi}{4}) \\ -\sin(\frac{\pi}{4}) & \cos(\frac{\pi}{4}) \end{bmatrix} \begin{bmatrix} 1 & 0 \\ 0 & e^{i\Delta\phi_2} \end{bmatrix} \begin{bmatrix} \cos(-\frac{\pi}{4}) & \sin(-\frac{\pi}{4}) \\ -\sin(-\frac{\pi}{4}) & \cos(-\frac{\pi}{4}) \end{bmatrix}$$

$$\begin{bmatrix} \cos(-\frac{\pi}{4}) & \sin(-\frac{\pi}{4}) \\ -\sin(-\frac{\pi}{4}) & \cos(-\frac{\pi}{4}) \end{bmatrix} \begin{bmatrix} 1 & 0 \\ 0 & e^{i\Delta\phi_1} \end{bmatrix} \begin{bmatrix} \cos(\frac{\pi}{4}) & \sin(\frac{\pi}{4}) \\ -\sin(\frac{\pi}{4}) & \cos(\frac{\pi}{4}) \end{bmatrix} E_i$$

where $E_i = \begin{bmatrix} 1 \\ 0 \end{bmatrix} E_0 e^{-i(kz-\omega t)}$. These matrices represent the effect of each cell on the light passing through the cell. Each display is given by the product of three matrices as follows:

$$\begin{bmatrix} \cos(-\frac{\pi}{4}) & \sin(-\frac{\pi}{4}) \\ -\sin(-\frac{\pi}{4}) & \cos(-\frac{\pi}{4}) \end{bmatrix} \begin{bmatrix} 1 & 0 \\ 0 & e^{i\Delta\phi} \end{bmatrix} \begin{bmatrix} \cos(\frac{\pi}{4}) & \sin(\frac{\pi}{4}) \\ -\sin(\frac{\pi}{4}) & \cos(\frac{\pi}{4}) \end{bmatrix}$$

The first matrix is the coordinate rotation matrix with clockwise rotation of the optical axis, i.e. $(\theta = \frac{\pi}{4})$. The last matrix represents the coordinate rotation matrix with an

anticlockwise rotation of the optical axis ($\theta = -\frac{\pi}{4}$). The second matrix is the retardation matrix, representing the difference in phase shift $\Delta\phi$ introduced by the LC cell as a result of the applied voltage. These phase shifts $\Delta\phi_2$ and $\Delta\phi_1$ can vary continuously with applied voltage. This matrix Equation can be simplified to:

$$E_t = \begin{bmatrix} 1 \\ 0 \end{bmatrix} \cos\left(\frac{\Delta\phi_1 - \Delta\phi_2}{2}\right) \exp\left[i\left(\frac{\Delta\phi_1 + \Delta\phi_2}{2}\right)\right] E_0 e^{-i(kz-\omega t)}.$$

The term $\cos\left(\frac{\Delta\phi_1 - \Delta\phi_2}{2}\right)$ represents the amplitude modulation induced while the term, $\psi = \frac{\Delta\phi_1 + \Delta\phi_2}{2}$ represents the induced phase shift. If $\Delta\phi_1 = -\Delta\phi_2$ only amplitude modulation is induced by the SLM while if $\Delta\phi_1 = \Delta\phi_2$ then only phase modulation is induced by the SLM.

2.4 Nonlinear optical effects

When high intensity light propagates through certain materials, the materials optical properties can become a function of intensity [24]. The nonlinear optics is the study of phenomena that occur as a consequence of the modification of the optical properties of a material system by the presence of light [4].

The characterization of ultra-short laser pulses is difficult since no electronics exist that can measure such short time durations. Several methods, mostly using nonlinear optical effects, have been developed to characterize ultra-short pulses. These include background free autocorrelation, frequency resolved optical gating (FROG) and the spectral interferometry for direct electric field reconstruction (SPIDER). All these techniques employ nonlinear optical effects to measure the pulse duration of an ultra-short laser pulse.

2.4.1 Interaction of light with matter

The interaction of light with any medium is governed by Maxwell's Equations which are given by [4]

$$\nabla \times \mathbf{H} = \frac{1}{c}\frac{\partial \mathbf{D}}{\partial t} + \frac{4\pi}{c}\mathbf{j}, \tag{2.17}$$

$$\nabla \times \mathbf{E} = -\frac{1}{c}\frac{\partial \mathbf{B}}{\partial t}, \tag{2.18}$$

where $\mathbf{j}$ is the electric current density and c is the speed of light in vacuum. The relationship between the electric displacement field $\mathbf{D}$, the polarization $\mathbf{P}$ and the electric field strength $\mathbf{E}$ is given by:

$$\mathbf{D} = \mathbf{E} + 4\pi\mathbf{P}. \tag{2.19}$$

Applying the operator (∇) to Equation (2.18) and replacing $(\nabla \times \mathbf{H})$ by its expression from Equation (2.17), we obtain the following Equation;

$$\nabla \times (\nabla \times \mathbf{E}) = -\frac{1}{c^2}\frac{\partial^2 \mathbf{D}}{\partial t^2} + \frac{4\pi}{c^2}\frac{\partial \mathbf{j}}{\partial t}, \tag{2.20}$$

Substituting Equation (2.19) in Equation (2.20) and taking into account the non-conductive property of the material ($\mathbf{j} = 0$), we have

$$\nabla \times (\nabla \times \mathbf{E}) + \frac{1}{c^2}\frac{\partial^2 \mathbf{E}}{\partial t^2} = -\frac{4\pi}{c^2}\frac{\partial^2 \mathbf{P}}{\partial t^2}. \tag{2.21}$$

The left hand side of this Equation defines the wave Equation used in vacuum while the right hand side represents the source term and contains the induced polarization changes in a medium. The wave Equation (2.21) is the general form used for all media and can be modified to describe the response of the specific medium.

2.4.2 Nonlinear propagation

When light propagates through a medium, it induces a polarization in the medium. The polarization P is responsible for all optical phenomena that occur in the medium. This polarization P is a function of the incident electric field strength, E. In general, the

polarization can be described as the sum of increasing orders of polarization [5]:

$$P = p^{(1)} + p^{(2)} + p^{(3)} + \cdots p^{(i)}; \tag{2.22}$$

where $p^{(i)}$ represents the $i - th$ order of the polarization. In terms of the electric field strength and optical susceptibilities, χ, Equation (2.22) can be written as

$$P = \varepsilon_0 \chi^{(1)} E + \varepsilon_0 \left(\chi^{(2)} E^2 + \chi^{(3)} E^3 + \cdots \right), \tag{2.23}$$

where ε_0 is the permittivity of free space and $\chi^{(i)}$ is the $i - th$ order optical susceptibility.

The optical susceptibilities, $\chi^{(i)}$ are in general tensors of rank $n = i$. They describe the response of the medium and incident electromagnetic field.

At low incident intensities, the higher order terms of Equation 2.23 become insignificant and the response of the medium is describe by the first term (linear term). This is the realm of linear optics [12]

$$p^L = \epsilon_0 \chi^{(1)} E, \tag{2.24}$$

where $\chi^{(1)}$ is the linear optical susceptibility. If the intensity of the incident light is high enough, the higher order terms of Equation (2.23) must be considered as well. The polarization can then be written as sum of the linear contribution p^L and the nonlinear contribution p^{NL},

$$P = p^L + p^{NL}, \tag{2.25}$$

where,

$$p^{NL} = \epsilon_0 \left(\chi^{(2)} EE + \chi^{(3)} EEE + \cdots \right), \tag{2.26}$$

where $\chi^{(2)}$, $\chi^{(3)}, \ldots$ are the nonlinear optical susceptibilities which depend on the frequency of the applied electric field and are responsible for all the nonlinear effects. One such nonlinear effect, which will be investigated in the next section, is second harmonic generation. The medium used for second harmonic generation in this case is a β-barium borate (BBO) crystal.

2.4.3 Second harmonic generation (SHG)

Second harmonic generation (SHG) is a nonlinear optical process in which an incident electric field with optical frequency ω, passes through a nonlinear material and generates a new electric field with optical frequency 2ω [5].

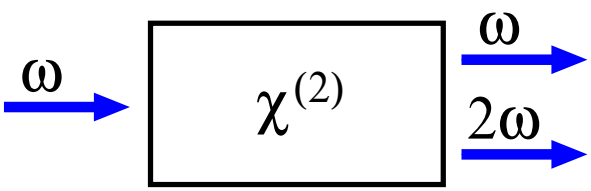

FIG. 2.5. Illustration of second harmonic generation in a crystal [5].

FIG. 2.5 illustrates this process in a crystal. It is the 2^{nd} order polarization which is responsible for the generation of the second harmonic signal, i.e.

$$p^{(2)}(t) = \epsilon_0 \chi^{(2)} E^2(t). \tag{2.27}$$

This Equation can be rewritten, using the definition of the electric field given in Equation (2.1), to indicate the origin of the second harmonic frequency

$$p^{(2)}(t) = \varepsilon_0 \chi^{(2)} E_0^2 \exp\left[-2i(kz - \omega t)\right], \tag{2.28}$$

Equation (2.28) produces second order polarization which has a contribution at 2ω frequency. In accordance with the propagated wave Equation (2.21), the contribution of Equation (2.28) can act as a source for the generation of electromagnetic radiation at the second harmonic frequency [5].

2.5 Fourier transform (FT)

The Fourier transform is defined as a mathematical operation decomposing a signal into its corresponding constituent frequencies. It is mainly used in communication systems and electrical networks studies [16]. In this study, Fourier transformations on two different domains were investigated. The Fourier transform from time to optical frequency was

investigated both analytically and numerically, whilst the Fourier transform from spatial coordinates to spatial frequency coordinates was investigated numerically.

The temporal signal investigated was a Gaussian laser pulse described by

$$E(t) = E_0 \exp\left[-\left(\frac{t}{\sigma}\right)^2\right] \exp(iw_0 t). \tag{2.29}$$

The first exponential term describes the Gaussian envelope of the pulse while the second exponential describes the oscillation of the electric field inside the envelope, with a constant phase equal to zero, ($\psi_0 = 0$). The amplitude E_0 is computed by normalizing the electric field with regards to the total energy in the pulse. The normalization of the electric field $E(t)$ is done using the following formula:

$$\int_{-\infty}^{+\infty} E(t)E^*(t)dt = 1,$$

where $E^*(t)$ is the complex conjugate of $E(t)$. It can be shown that E_0 is given by

$$E_0 = \frac{1}{\sqrt{\sigma}} \left(\frac{2}{\pi}\right)^{\frac{1}{4}}. \tag{2.30}$$

Substituting Equation (2.30) into (2.29), the electric field is given by:

$$E(t) = \frac{1}{\sqrt{\sigma}} \left(\frac{2}{\pi}\right)^{\frac{1}{4}} \exp\left(-(\frac{t}{\sigma})^2\right) \exp(iw_0 t). \tag{2.31}$$

Equation (2.31) is complex, and it is often useful (for instance when plotting the electric field) to only consider the real part of $\exp(iw_0 t)$ term:

$$\exp(iw_0 t) = \cos(w_0 t) + i \sin(w_0 t). \tag{2.32}$$

This results in $E(t)$ being rewritten as [10]:

$$E(t) = \frac{1}{\sqrt{\sigma}} \left(\frac{2}{\pi}\right)^{\frac{1}{4}} \exp\left[-(\frac{t}{\sigma})^2\right] \cos(w_0 t), \tag{2.33}$$

where σ is the pulse duration and $w_0 = \frac{2\pi c}{\lambda}$ is the central frequency with c the speed of light.

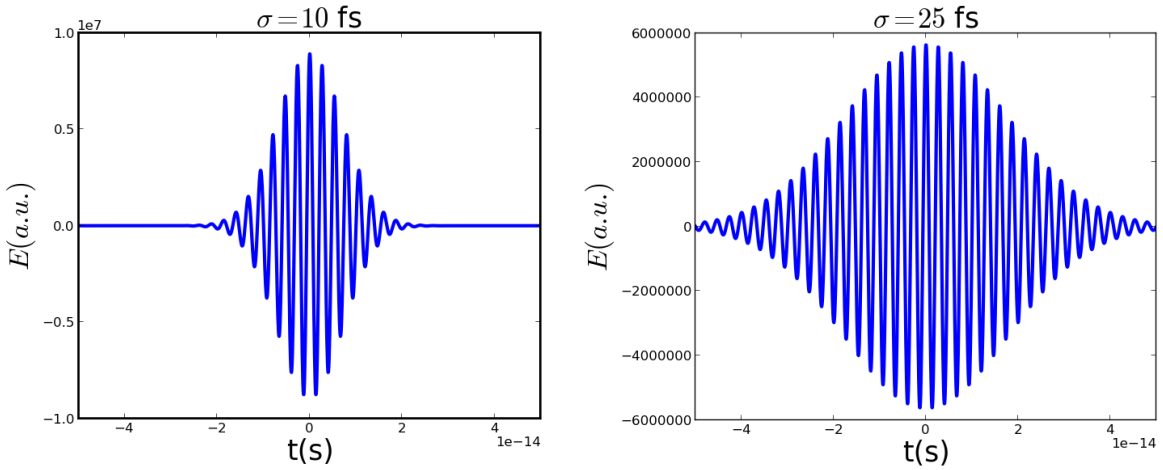

(a) (b)

FIG. 2.6. Plots of Equation (2.33) for two different values of σ, namely $\sigma = 10$ fs (a) and $\sigma = 25$ fs (b).

All the simulations in this work were done using Python as programming language [21, 27]. The parameter values for the simulations are provided in TABLE. 2.1. Equation 2.33 is plotted in FIG. 2.6 for different values of pulse duration, σ (10 FIG. 2.6(a) and 25 fs FIG. 2.6(b)). The values of the different pulse widths were selected in order to illustrate the physical nature of a Gaussian laser pulse. FIG. 2.6 depicts the oscillation of the

Speed of light: c	3×10^8	m/s
Central frequency: ω_0	2.355×10^{15}	Hz
time interval: t	$[-6 \times 10^{-13}, 6 \times 10^{-13}]$	s
Frequency interval: ω	$[1.7 \times 10^{15}, 3.0 \times 10^{15}]$	Hz
Pulse duration: σ	10, 25	fs
Time delay: τ	300	fs
Number of points	18000	

TABLE. 2.1. Values of the parameters used in the simulation.

electric field inside the Gaussian envelope. The oscillations and envelope move together with a group velocity (V_g). The V_g is given by the derivative of the angular frequency with respect to the wave number:

$$V_g = \frac{\partial \omega}{\partial k}. \tag{2.34}$$

2.5.1 Analytical study of FT

The Fourier transform of the electric filed in the time domain, $E(t)$, is given by the electric field in the frequency domain, $\tilde{E}(\omega)$. Performing an inverse Fourier transform on $\tilde{E}(\omega)$ results in an electric field in the time domain, $E'(t)$. We employ analytical calculations to perform these respective Fourier transformations according to the following formula [10]:

$$\tilde{E}(\omega) = \int_{-\infty}^{+\infty} E(t) \exp(-iwt) dt, \tag{2.35}$$

$$E'(t) = K \int_{-\infty}^{+\infty} \tilde{E}(\omega) \exp(iwt) d\omega, \tag{2.36}$$

where K is a constant that can be chosen in order to ensure conservation of energy. These expressions look very similar with the only difference being the sign that appears in the exponent. We will first consider the Fourier transform of a single Gaussian pulse, before considering a double pulse.

2.5.1.1 Fourier transform of a single Gaussian pulse

Let us consider the Equation for a Gaussian pulse described by Equation (2.33), as well as the identity shown in Equation (2.32). Inserting these Equations into Equation (2.35) we obtain:

$$\tilde{E}(\omega) = \int_{-\infty}^{+\infty} \frac{1}{\sqrt{\sigma}} \left(\frac{2}{\pi}\right)^{\frac{1}{4}} \exp\left(-\left(\frac{t}{\sigma}\right)^2\right) \cos(\omega_0 t) \left[\cos(\omega t) + i \sin(\omega t)\right] dt. \tag{2.37}$$

If we notice that the integral of the product $\cos(\omega_0 t) \sin(\omega t)$ is zero for values of t $(-\infty, +\infty)$, and by applying the following trigonometric transformation of the product $\cos(\omega_0 t) \cos(\omega t)$

$$\cos(\omega_0 t) \cos(\omega t) = \frac{1}{2} \left[\cos(\omega_0 + \omega)t + \cos(\omega_0 - \omega)t\right], \tag{2.38}$$

we can write (2.37) as:

$$\tilde{E}(\omega) = \frac{1}{2\sqrt{\sigma}} \left(\frac{2}{\pi}\right)^{\frac{1}{4}} \int_{-\infty}^{+\infty} E(t) \exp\left[-\left(\frac{t}{\sigma}\right)^2\right] \left(\cos\left[(w_0 + w)t\right] + \cos\left[(w_0 - w)t\right]\right) dt. \tag{2.39}$$

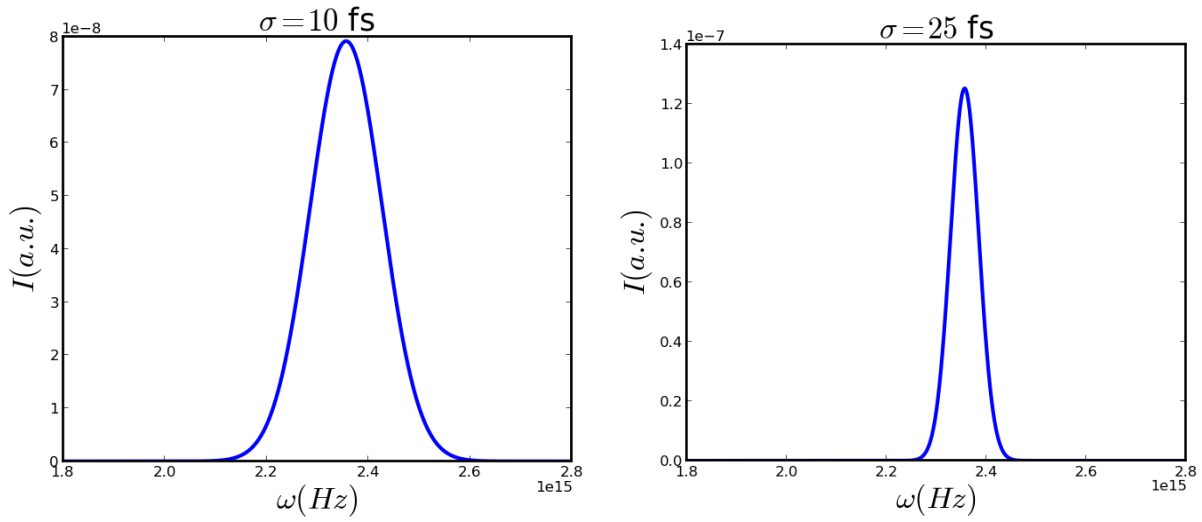

(a) (b)

FIG. 2.7. Intensity I(ω) spectrum of the electric field in frequency domain for two different values of σ; 10 fs (a) and 25 fs (b).

Using the following form of integral [6],

$$\int_{-\infty}^{+\infty} \exp\left[-(at)^2\right] \cos(\gamma t) dt = \frac{\sqrt{\pi}}{a} \exp\left(-\left(\frac{\gamma}{a}\right)^2\right), \tag{2.40}$$

with $a = \frac{1}{\sigma}$ and $\gamma = \omega_0 \pm \omega$, Equation (2.39) is then reduced to

$$\tilde{E}(\omega) = \frac{\sqrt{\sigma\pi}}{2} \left(\frac{2}{\pi}\right)^{\frac{1}{4}} \exp\left[-(\sigma(w_0 - w))^2\right] \left[1 - \exp\left(-\sigma^2 \omega_0 \omega\right)\right].$$

The exponential of a large negative value is negligible so that $\exp(-\sigma^2\omega_0\omega) \approx 0$. This leads to

$$\tilde{E}(\omega) = \frac{\sqrt{\sigma\pi}}{2} \left(\frac{2}{\pi}\right)^{\frac{1}{4}} \exp\left[-(\sigma(w_0 - w))^2\right]. \tag{2.41}$$

The intensity profile of an electric field is given by the square of the absolute value of the electric field (Equation (2.41)):

$$I(\omega) = |\tilde{E}(\omega)|^2 . \tag{2.42}$$

To illustrate, we plot Equation (2.42) for two different values of the pulse duration, σ, in FIG. 2.7.

FIG. 2.7 shows that for a large (or small) value of the pulse duration σ in the time domain,

the width of the pulse narrow (or broad) in the frequency domain. This argument is supported by the relationship between the pulse duration and the spectral bandwidth for a Fourier limited pulse. Both are inversely proportional as shown in the following Equation [24]:

$$\sigma\Delta\omega = s. \tag{2.43}$$

The value of the constant s depends on the pulse shape. For a Gaussian shape, the value is $s = 0.44$.

By applying the inverse FT in Equation (2.36) to Equation (2.41), we can again transform the pulse from frequency domain back into time domain as follows:

$$E'(t) = K\int_{-\infty}^{+\infty}\frac{\sqrt{\sigma\pi}}{2}\left(\frac{2}{\pi}\right)^{\frac{1}{4}}\exp\left[-\left(\sigma(\omega_0-\omega)\right)^2\right]\left[\cos(\omega t)+i\sin(\omega t)\right]d\omega. \tag{2.44}$$

Since the integral of a sin function over all space is zero, the sin part is neglected. By changing variables such as $\omega = \omega_0 - X$ and $d\omega = -dX$ and also choosing $K = \frac{2}{\pi}$, we get the following expression:

$$E'(t) = -\frac{\sqrt{\sigma\pi}}{\pi}\left(\frac{2}{\pi}\right)^{\frac{1}{4}}\cos(\omega_0 t)\int_{-\infty}^{+\infty}\exp\left[-\left(\frac{\sigma X}{2}\right)^2\right]\cos(Xt)dX\ .$$

Using Equation (2.40), $E'(t)$ is expressed as:

$$E'(t) = -\frac{1}{\sqrt{\sigma}}\left(\frac{2}{\pi}\right)^{\frac{1}{4}}\exp\left[-\left(\frac{t}{\sigma}\right)^2\right]\cos(\omega_0 t). \tag{2.45}$$

When on compares Equation (2.45) with Equation (2.33), it can be seen that the Equations are the same, except for a minus sign, which only introduces a fixed phase shift. This indicates that transforming back and forth between time and frequency can be done without any loss of information. The result of the inverse Fourier transform (Equation (2.45)) is plotted in FIG. 2.8(a), (b) for two different pulse widths.

2.5.1.2 Fourier transform of two Gaussian pulses (double pulse)

We examine the Fourier transform of two Gaussian pulses (double pulse) using the same procedure employed for the single Gaussian pulse. The two pulses under investigation are

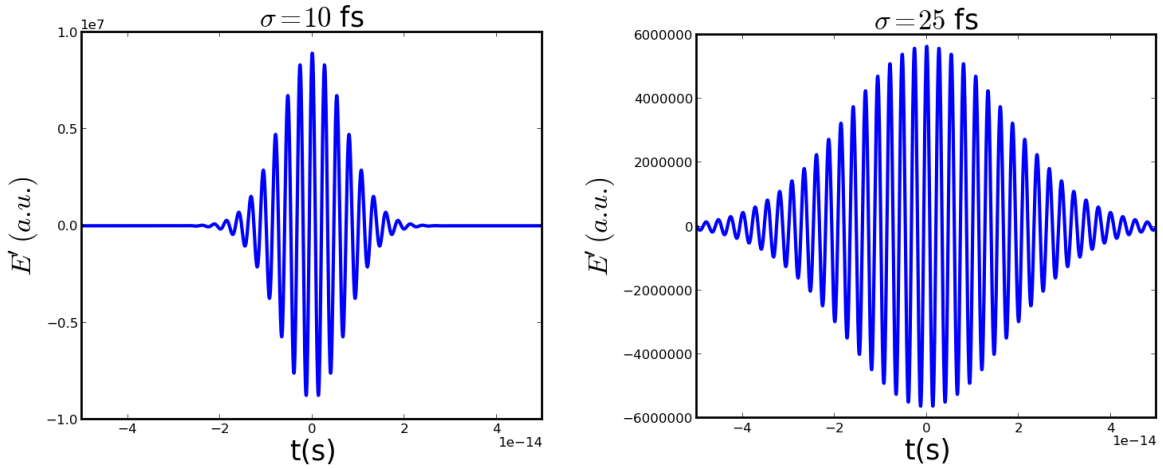

(a) (b)

FIG. 2.8. Plots of Equation (2.45), showing the inverse FT of the electric field in frequency domain, for two different pulse lengths σ; 10 fs (a) and 25 fs (b).

separated by $T = 2\tau$ (with $\tau = 150$ fs). The function investigated is given by

$$E_1(t) = \frac{1}{\sqrt{\sigma}}\left(\frac{2}{\pi}\right)^{\frac{1}{4}}\left(\exp\left[-\left(\frac{t+\tau}{\sigma}\right)^2\right]\cos[\omega_0(t+\tau)] + \exp\left[-\left(\frac{t-\tau}{\sigma}\right)^2\right]\cos[\omega_0(t-\tau)]\right) \tag{2.46}$$

FIG. 2.9 depicts the function described in Equation (2.46). It represents the two pulses separated by $T = 300$ fs. If we now apply a Fourier transformation on Equation (2.46) we obtain

$$\begin{aligned}\tilde{E}_1(\omega) = &\int_{-\infty}^{+\infty}\frac{1}{\sqrt{\sigma}}\left(\frac{2}{\pi}\right)^{\frac{1}{4}}\exp\left(-\left(\frac{t+\tau}{\sigma}\right)^2\right)\cos[\omega_0(t+\tau)]\cos(\omega t)\\ &+\int_{-\infty}^{+\infty}\frac{1}{\sqrt{\sigma}}\left(\frac{2}{\pi}\right)^{\frac{1}{4}}\exp\left(-\left(\frac{t-\tau}{\sigma}\right)^2\right)\cos[\omega_0(t-\tau)]\cos(\omega t)dt.\end{aligned} \tag{2.47}$$

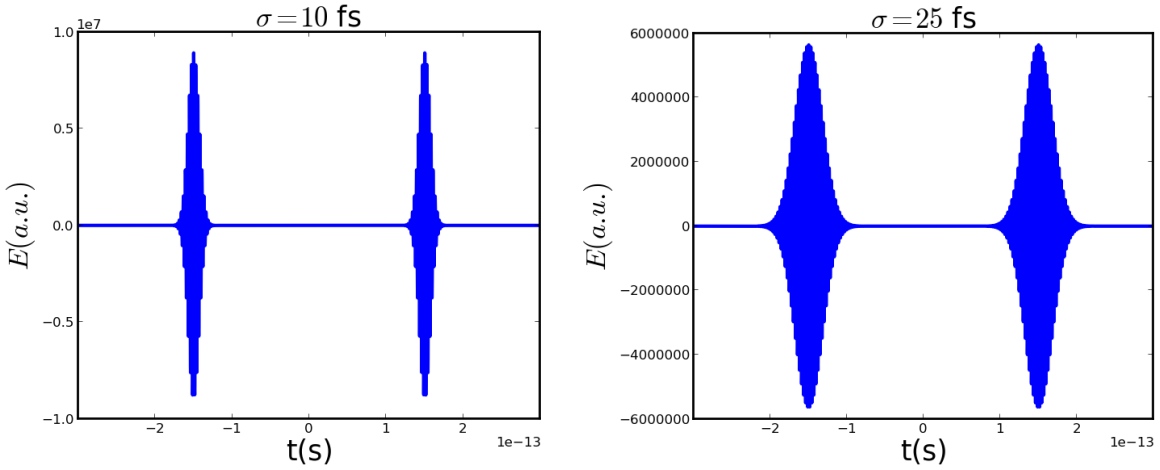

(a) (b)

FIG. 2.9. Plot of Equation (2.46) of two Gaussian pulses separated by $T = 300$ fs for $\sigma = 10$ fs (a) and $\sigma = 25$ fs (b).

By performing the following transformations, $x = t - \tau$, $y = t + \tau$, we obtain $dx = dy = dt$, and Equation (2.47) becomes

$$\begin{aligned}\tilde{E}_1(\omega) = &\frac{1}{\sqrt{\sigma}}\left(\frac{2}{\pi}\right)^{\frac{1}{4}}\int_{-\infty}^{+\infty}\exp\left(-\left(\frac{x}{\sigma}\right)^2\right)\cos(\omega_0 x)\cos[\omega(x+\tau)]dx \\ &+\frac{1}{\sqrt{\sigma}}\left(\frac{2}{\pi}\right)^{\frac{1}{4}}\int_{-\infty}^{+\infty}\exp\left(-\left(\frac{y}{\sigma}\right)^2\right)\cos(\omega_0 y)\cos[\omega(y-\tau)]dy.\end{aligned} \tag{2.48}$$

Using trigonometric identities and neglecting the sine part as we did previously, Equation (2.38) can be written as:

$$\begin{aligned}\tilde{E}_1(\omega) = &\frac{1}{2\sqrt{\sigma}}\left(\frac{2}{\pi}\right)^{\frac{1}{4}}\cos(\omega\tau)\int_{-\infty}^{+\infty}\exp\left(-\left(\frac{x}{\sigma}\right)^2\right)\left(\cos\left[(\omega_0+\omega)x\right]+\cos\left[(\omega_0-\omega)x\right]\right)dx \\ &+\frac{1}{2\sqrt{\sigma}}\left(\frac{2}{\pi}\right)^{\frac{1}{4}}\cos(\omega\tau)\int_{-\infty}^{+\infty}\exp\left(-\left(\frac{y}{\sigma}\right)^2\right)\left(\cos\left[(\omega_0+\omega)y\right]+\cos\left[(\omega_0-\omega)y\right]\right)dy.\end{aligned} \tag{2.49}$$

Since the two integrals in the above Equation have the same limits of integration. It is possible to add the two integrals. Using Equation (2.40), we have

$$\tilde{E}_1(\omega) = \frac{2\sigma\sqrt{\pi}}{2\sqrt{\sigma}}\left(\frac{2}{\pi}\right)^{\frac{1}{4}}\cos(\omega\tau)\left[\exp\left(-[\sigma(\omega_0+\omega)]^2\right)+\exp\left(-[\sigma(\omega_0-\omega)]^2\right)\right].$$

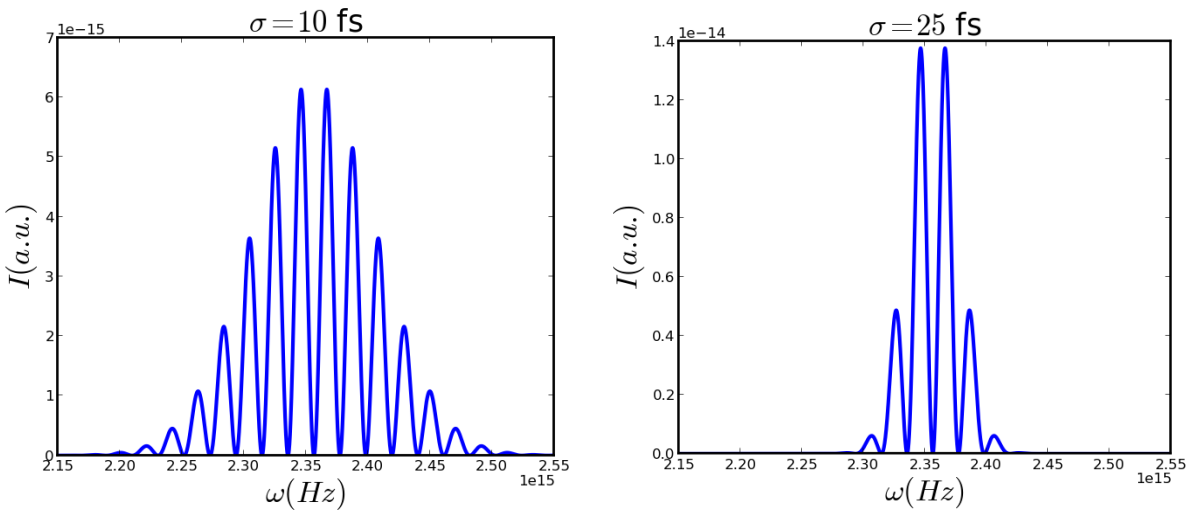

(a) (b)

FIG. 2.10. Intensity of the Fourier transform of a double Gaussian pulse for a pulse duration of 10 fs (a) and 25 fs (b).

$$\tilde{E}_1(\omega) = \sqrt{\pi\sigma}\left(\frac{2}{\pi}\right)^{\frac{1}{4}} \cos(\omega\tau)\exp\left(-[\sigma(\omega_0-\omega)]^2\right)\left[1+\exp\left([\sigma(\omega_0-\omega)]^2-[\sigma(\omega_0+\omega)]^2\right)\right]. \tag{2.50}$$

Equation (2.50) can be rewritten as :

$$\tilde{E}_1(\omega) = \sqrt{\pi\sigma}\left(\frac{2}{\pi}\right)^{\frac{1}{4}} \cos(\omega\tau)\exp\left(-[\sigma(\omega_0-\omega)]^2\right)\left(1+\exp(-4\sigma^2\omega_0\omega)\right). \tag{2.51}$$

We obtain the final expression of $\tilde{E}_1(\omega)$ by again neglecting the term $\exp(-4\sigma^2\omega_0\omega)$

$$\tilde{E}_1(\omega) = \sqrt{\pi\sigma}\left(\frac{2}{\pi}\right)^{\frac{1}{4}} \cos(\omega\tau)\exp\left(-[\sigma(\omega_0-\omega)]^2\right), \tag{2.52}$$

The intensity is given by

$$I_1(\omega) = |\tilde{E}_1(\omega)|^2. \tag{2.53}$$

It can be clearly seen in FIG 2.10(a), (b) that the spectrum of the double Gaussian pulse is the same as that of a single pulse, but with a frequency modulation. The modulation has a frequency proportional to the inverse of the separation between the two pulses, $1/\tau$. This means that the further the pulses are apart, the closer the spacing of the fringes will be. Now we again perform the inverse Fourier transform by inserting Equation (2.52) into

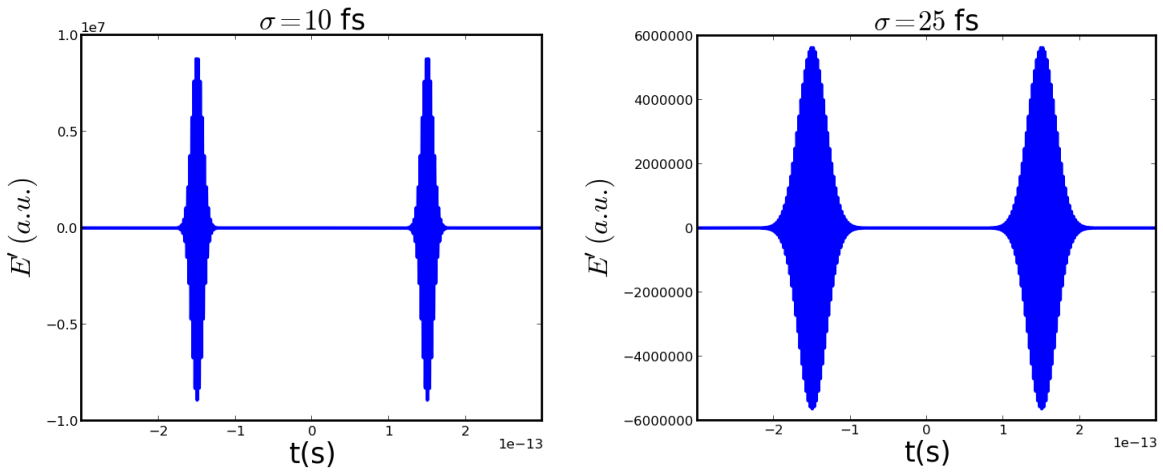

(a) (b)

FIG. 2.11. Plots of the inverse Fourier transform of the spectrum of a double pulse $\tilde{E}_1(\omega)$ (separated by 300 fs) for different sigma: 10 (a) and 25 fs (b).

the inverse Fourier transform Equation (2.36), to obtain

$$E_1'(t) = K \int_{-\infty}^{+\infty} \sqrt{\pi\sigma} \left(\frac{2}{\pi}\right)^{\frac{1}{4}} \cos(\omega\tau) \exp\left[-(\sigma[\omega_0 - \omega])^2\right] \cos(\omega t) d\omega. \tag{2.54}$$

By changing the variables $y = \omega_0 - \omega$ we have $d\omega = -dy$. Then $E_1'(t)$ is given by

$$E_1'(t) = -\frac{2}{\pi}\sqrt{\pi\sigma} \left(\frac{2}{\pi}\right)^{\frac{1}{4}} \int_{-\infty}^{+\infty} \cos([\omega_0 - y]\tau) \cos([\omega_0 - y]t) \exp\left[-(\sigma y)^2\right] dy. \tag{2.55}$$

Using trigonometric identities and applying Equation (2.40), $E_1'(t)$ can be rewritten as:

$$E_1'(t) = -\frac{1}{\sqrt{\sigma}} \left(\frac{2}{\pi}\right)^{\frac{1}{4}} \left(\cos(\omega_0[t+\tau]) \exp\left(-\left(\frac{t+\tau}{\sigma}\right)^2\right) + \cos(\omega_0[t-\tau]) \exp\left(-\left(\frac{t-\tau}{\sigma}\right)^2\right)\right). \tag{2.56}$$

Looking at Equation (2.56), it can be seen that the inverse Fourier transform has produced the original pulse in time domain. This is also illustrated in FIG. 2.11. All the original information in the pulse is preserved through these transformations. All these calculations were performed analytically. The same analysis is also performed numerically in Chapter 4. In the next section, we will see how the Fourier transform can also be applied to the spatial and spatial frequency domains. This is of use when trying to model the complete $4f$-pulse shaper using Fourier optics.

2.6 Modeling of the $4f$-pulse shaper in space and spatial frequency using Fourier optics

A $4f$-pulse shaper with a computer controlled SLM can control the phase, amplitude and frequency of an optical pulse that passes through such a system [17]. In this section, we develop the tools necessary to model the propagation of the beam through the $4f$-pulse shaper. This system deals with two consecutive Fourier transform from space to spatial frequency. The first lens performs the Fourier transform at the focal planes: planes of the first grating and midway between the two lenses (i.e., back focal plane of L_1). The second lens also performs a FT from the midway plane to the second grating plane (i.e., back focal plane of L_2) [29]. This makes the incoming pulse unchanged when propagating through the system without the Spatial Light Modulator (SLM) [30]. As can be seen, each optical component is placed one focal length $f = 25$ cm from the previous component. This results in the so-called $4f$-geometry.

In the $4f$-pulse shaper, the first grating disperses each wavelength component in a different direction. The first lens collimates the beam and ensures that each wavelength component is well separated from the other at the position of the SLM. The second lens refocuses all the wavelength components onto the second grating, which recombines all the wavelengths into a single beam. If the SLM does nothing to the pulse, then the incident pulse and the exit pulse should be exactly the same. Since diffraction will only occur in the x-plane and we are using cylindrical lenses (only focusing in the x-plane) we only have to consider one spatial dimension which simplifies matters considerably. We initially only consider the two lens system in the next section (as shown in FIG 2.12) before introducing the gratings in the following section.

2.6.1 Modeling of the $4f$-pulse shaper without gratings

Since we have no dispersive elements in this analysis, we consider only a monochromatic laser beam with a Gaussian spatial distribution. The beam propagating in the z-direction

is described by [8]

$$E_G(x) = A(z)\exp\left[-\left(\frac{x}{w(z)}\right)^2 - ikz - \frac{ikx^2}{2R(z)} + i\phi(z)\right], \tag{2.57}$$

where $w(z) = w_0\sqrt{1+(\frac{z}{z_0})^2}$ is the beam width, $A(z) = A_0\left(\sqrt{1+(\frac{z}{z_0})^2}\right)^{-\frac{1}{4}}$ is the amplitude (with $z_0 = \frac{\pi w_0^2}{\lambda}$ the Rayleigh length) and w_0 is the beam waist. $R(z) = z\left(1+(\frac{z_0}{z})^2\right)$ is the radius of curvature and $\phi(z) = \frac{1}{2}arc\tan(\frac{z}{z_0})$, is the Gouy phase and k is the wave number. Equation (2.57) represents a Gaussian profile, which is considered as the incident beam on the system.

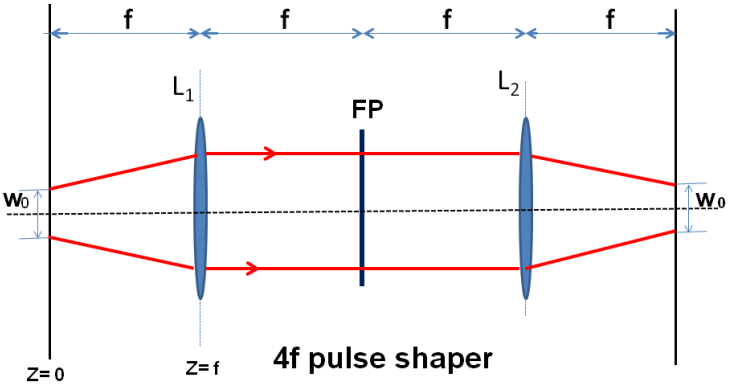

FIG. 2.12. Schematic of the Gaussian pulse travelling through the $4f$-pulse shaper without gratings.

As can be seen in FIG. 2.12, we consider the beam at position $z = 0$ to be at its waist meaning the radius of curvature is infinite ($R(0) = \infty$) and the Gouy phase is zero ($\phi(z) = \frac{1}{2}arc\tan(\frac{z}{z_0}) = 0$) [11]. The Equation describing our Gaussian distribution then becomes

$$E_G(x) = A_0\exp\left[-\left(\frac{x}{w_0}\right)^2\right]. \tag{2.58}$$

The principle of Fourier optics boils down to representing each optical element as a specific transfer function, applied to the spatial distribution of the input pulse (it is important to realize that free space propagation is also considered an optical element in this approach). This transformation can be done either in the spatial or spatial frequency domains, depending on the specific optical element under consideration. The two transfer functions

of importance in this section, are that of free space propagation (which acts in the spatial frequency domain) and the lens (which acts in the spatial domain).

The free space transfer function can be expressed as:

$$H(f_x) = \exp\left(jkz\sqrt{1-(\lambda f_x)^2}\right) \ . \tag{2.59}$$

This free space propagation is derived from the diffraction at boundaries by applying a complex representation of a plane wave which is given by [16]

$$P(x,z;t) = \exp\left(j(\mathbf{kr} - 2\pi\nu)\right) \ . \tag{2.60}$$

The term $\sqrt{1-(\lambda f_x)^2}$ of Equation 2.59 is derived from the complex time independent plane wave $P(x,z) = \exp(j\mathbf{kr}) = \exp\left(j\frac{2\pi}{\lambda}(\alpha x + \gamma z)\right)$ with $\mathbf{r} = x\hat{x} + z\hat{z}$ the position vector and $\mathbf{k} = \frac{2\pi}{\lambda}(\alpha\hat{x} + \gamma\hat{z})$ the wave vector function of direction (α,γ) with the magnitude $\frac{2\pi}{\lambda}$. This means that the module $|\alpha\hat{x} + \gamma\hat{z}|$ must be one, implying that $\gamma = \sqrt{1-\alpha^2}$. At the $z = 0$ plane, the complex exponential function $\exp(j2\pi f_x x)$ compared to the plane wave expression $P(x,0)$ leads to the relationship between the propagation direction of the plane wave and the spatial frequency (f_x) as $\alpha = \lambda f_x$, $\gamma = \sqrt{1-(\lambda f_x)^2}$.

The next element to consider is the lens. It acts in the spatial domain and is given by

$$U_l(x) = \exp\left(jk\Delta_0\right)\exp\left(jk(n-1)\Delta(x)\right) \ , \tag{2.61}$$

where Δ_0 is the maximum thickness, $\Delta(x) = \Delta_0 - \frac{x^2}{2}(\frac{1}{R1} - \frac{1}{R2})$ is the thickness at coordinate x, n is the refractive index of the lens and R_1 and R_2 are the radius of curvature of the two surfaces of the lens. A lens is a dense optical material which introduces phase delay $k(\Delta_0 - \Delta(x))$ across the beam. By substituting $\Delta(x)$ into Equation (2.61) and considering the focal length of the lens to be $f = (\eta - 1)(\frac{1}{R1} - \frac{1}{R2})$, and lastly by omitting the constant thickness term of the lens which only introduces a constant phase shift, the transfer function for the lens can be written as [16]:

$$U_l(x) = \exp\left(-\frac{jk}{2f}x^2\right) \ . \tag{2.62}$$

For this model, we start with a Gaussian beam at its waist position. The beam is then

Fourier transformed to the spatial frequency domain before being multiplied by the free space propagator. After propagating one focal length f, the beam is inverse Fourier transformed to the spatial domain and then multiplied with the lens transfer function. The beam is then again Fourier transformed to the spatial frequency domain before again being multiplied by the free space propagator. The beam has now been transferred to the position where the SLM would be located. This whole procedure is repeated for the second lens. For the results of this analysis, please refer to Chapter 4.

2.6.2 Modeling the $4f$-pulse shaper including gratings

For a complete model of the $4f$-pulse shaper, we need to include the 2 gratings as well. To do this model properly, we need to consider the polychromatic nature of our incident pulse. To illustrate the dispersive effect of the gratings, we consider three pulses of different wavelengths as our incident pulse. The distribution of the wavelengths within our $4f$-pulse shaper is illustrated in FIG. 2.13.

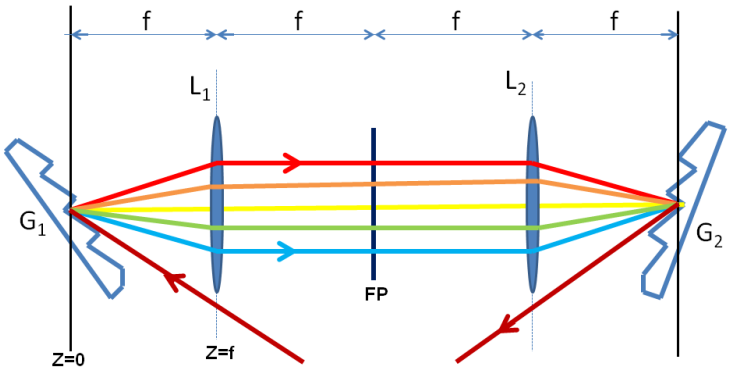

FIG. 2.13. Illustration of the wavelength distribution in the $4f$-pulse shaper.

The gratings are incorporated by introducing a grating transfer function. The grating transfer function works in the spatial domain and is defined as [11]

$$E_g(x) = \sqrt{b}\exp\left[jq(\omega-\omega_0)x\right], \tag{2.63}$$

where $b = \frac{\cos(i)}{\cos(\arcsin(\lambda_0/d-\sin(i)))}$ and $q = \frac{2\pi}{\omega_0 d\cos(\arcsin(\lambda_0/d-\sin(i)))}$ are constants depending on the angle of incidence i, d is the grating lines per mm.

The same procedure is followed as in the previous section, except that each of the three pulses of different wavelength is multiplied by the grating transfer function after the initial propagation (i.e., after G_1). The grating diffracts the different wavelengths into different angles, effectively changing the spatial frequencies of the different wavelength pulses. The field after the first grating $E_p(x)$ is expressed as the product of the grating and a Gaussian Equation

$$E_p(x) = E_g(x)E_G(x). \tag{2.64}$$

The angles of diffraction are related to the spatial frequency f_x according to:

$$\alpha_n = \lambda_n f_x, \tag{2.65}$$

where n is the number of the diffracted ray. Initially ($z = 0$), all the rays are on top of each other. The pulses of different wavelengths then propagate at different angles to the first lens, which collimates them. The second lens focuses the spatially separated but collimated wavelengths onto the second grating. Each of the wavelengths is incident at a different angle on the second grating. The grating recombines all the different wavelength components back into a single output pulse.

2.7 Autocorrelation techniques

In this section, we describe the characterization of ultra-short pulses using various autocorrelation techniques. Different techniques were developed for the characterization of ultra-short pulses in the femtosecond regime due to the incapability of opto-electronic devices to measure such short pulse durations. Autocorrelation techniques have many advantages, for instance the interferometric autocorrelator whose fringes act as its own calibration [20]. In general, autocorrelation is a technique whereby a signal is overlapped in a nonlinear fashion, with a delayed copy of itself. The output from an autocorrelator is a signal proportional to the square of the degree of overlap of the pulse and dependent on the delay between the pulses.

2.7.1 Intensity autocorrelation

The intensity autocorrelation, also called background-free autocorrelation, is suitable for measuring the pulse width. It is a relatively simple technique but the measurement contains no phase information. The pulse to be measured is split into 2 copies. The one copy is displaced and delayed with regards to the other copy. These two pulses are then overlapped non-collinearly in a non-linear crystal. The second harmonic signal produced in the forward direction is dependent on the delay between the two replicas [26]:

$$A^{(2)}_{BA}(\tau) = \int_{-\infty}^{+\infty} I(t-\tau)I(t)dt. \tag{2.66}$$

It is important to note that the information of the phase contained in electric field vanishes. A measurement using this technique was carried out and the result is discussed in Chapter 4.

2.7.2 Interferometric autocorrelation

The interferometric autocorrelation technique has the advantage that both the phase and intensity information is contained within the signal. The two replicas of the pulse to be measured are overlapped collinearly in a nonlinear medium. The result is a signal that contains interference fringes which also contain the phase information. The second order autocorrelation signal $A^{(2)}_{IA}(\tau)$ is defined as [10]:

$$A^{(2)}_{IA}(\tau) = \int_{-\infty}^{+\infty} \left[\left[E(t) + E(t-\tau)\right]^2\right]^2 dt. \tag{2.67}$$

Suppose that

$$G(\tau) = \left[\left[E(t) + E(t-\tau)\right]^2\right]^2, \tag{2.68}$$

by expanding Equation (2.68), we obtain

$$\begin{aligned} G(\tau) = &\left[E^4(t) + E^4(t-\tau) + 4E^2(t)E^2(t-\tau)\right] \\ &+4E(t)E(t-\tau)\left[E^2(t) + E^2(t-\tau)\right] + 2E^2(t)E^2(t-\tau). \end{aligned} \tag{2.69}$$

Since the intensity is a square of the electric field, given by Equation (2.29), the first term of $G(\tau)$ can be written as

$$G_1(\tau) = I^2(t) + I^2(t-\tau) + 4I(t)I(t-\tau). \tag{2.70}$$

$G_1(\tau)$ describes the second order autocorrelation phenomenon with its first two terms the constant background $I^2(t) + I^2(t-\tau)$, while the last two terms of Equation (2.69) result in the interference which contains the phase information.

2.7.3 Pulse shaper autocorrelation

The $4f$-pulse shaper was thoroughly described in the previous section (Section 2.6). In this section we describe how the $4f$-pulse shaper can be used to perform an autocorrelation measurement by mimicking the behaviour of an interferometric autocorrelator [15].

The advantage of this technique is that a measurement of the pulse shape can be performed at the position of an experiment, by exchanging the sample with a nonlinear crystal. The method is quite simple. By applying a sinusoidal transfer function to the SLM, it is possible to produce an exact copy of the incident pulse. By changing the period of the sinusoid, the separation between these copies can be varied. In this fashion, the pulses can be scanned across each other. If they are focused into a nonlinear crystal, a autocorrelation measurement can be performed. Since phases add linearly, it is possible to shape a pulse with the SLM, add the sinusoidal function to the applied phase and perform an autocorrelation measurement of the shaped pulse at the sample position. The sinusoidal function used in this study was [15]

$$T(\omega, \tau) = \cos\left[(\omega - (1-\gamma)\omega_c)\,\frac{\tau}{2}\right], \tag{2.71}$$

where ω is the angular frequency, ω_c is the carrier frequency and τ is the induced delay between the two pulses. For $\gamma = 0$ the carrier phase remains unchanged whilst for $\gamma = 1$, it shifts together with the envelope. This transfer function is investigated further, both numerically and experimentally, in Chapter 4.

Chapter 3

Experimental setups

This chapter describes the experimental setups and the methods implemented in the execution of the various experiments. The $4f$ pulse shaper is the setup used to modulate and characterize the pulses in our study, and hence special emphasis is placed on this setup. The setup for the investigation of polarization is presented and discussed in section 3.1. The techniques used to characterize short pulses are discussed in section 3.2. Section 3.3 describes the procedure by which the $4f$ pulse shaper is aligned.

3.1 Polarization control

The way in which the nature of the transmitted polarized light can be controlled using wave plates and a polarizer was investigated. The setup is shown in FIG. 3.1. A linearly polarized Helium-Neon (He-Ne) laser emitting at 632 nm was used as the source in these experiments since all the optics investigated were designed for the visible region of the spectrum. The optical axes of wave plates are parallel to the face of the wave plates. The effect of a half-wave plate and a quarter-wave plate on the polarization state of the incident light was investigated. The beam transmitted through the wave plate under investigation becomes the incident beam for a linear polarizer (analyzer). The light that passes through the analyzer then goes to a power meter (Coherent LM-2 VIS) where the total transmitted power is measured. For the first measurement we analyzed the polarization state of the light emitted from the laser source. This was done by measuring the transmitted light

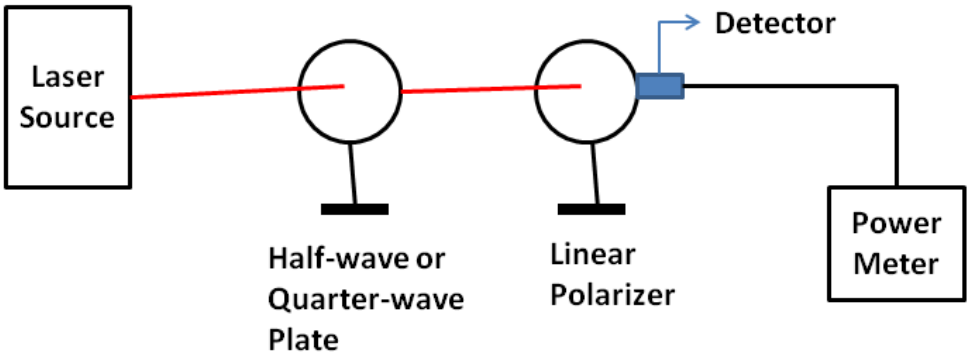

FIG. 3.1. Light polarization setup.

through the polarizer (no wave plate in the setup) as a function of polarizer angle. After the measurement, we then consecutively either inserted the half-wave plate or quarter-wave plate in front of the polarizer to investigate its influence on the polarization state of the light.

The respective wave plates were initially inserted such that their optical axes were parallel to the direction of the incident polarized beam. This was taken as their zero position. After that, one by one, each wave plate was rotated to specific angles (30° and 45° for the half-wave plate and 37.5° and 45° for the quarter-wave plate), while at each position the state of polarization was measured using the analyzer.

3.2 Pulse characterization

Three different second order autocorrelation techniques were investigated. These were background free intensity autocorrelation, interferometric autocorrelation and $4f$ pulse shaper assisted autocorrelation. In all cases a commercial Ti:Sapphire femtosecond laser (Spectra-Physics Tsunami) was used. The laser operated with a center wavelength of 800 nm, pulse energy of 10 nJ, pulse length of 75 ± 5 fs and pulse repetition rate of 80 MHz.

3.2.1 Intensity autocorrelation

The setup in FIG. 3.2 ensures that the measurement is able to produce experimental traces proportional to Equation (2.66). These traces come from the intensity of the pulse $I(t)$

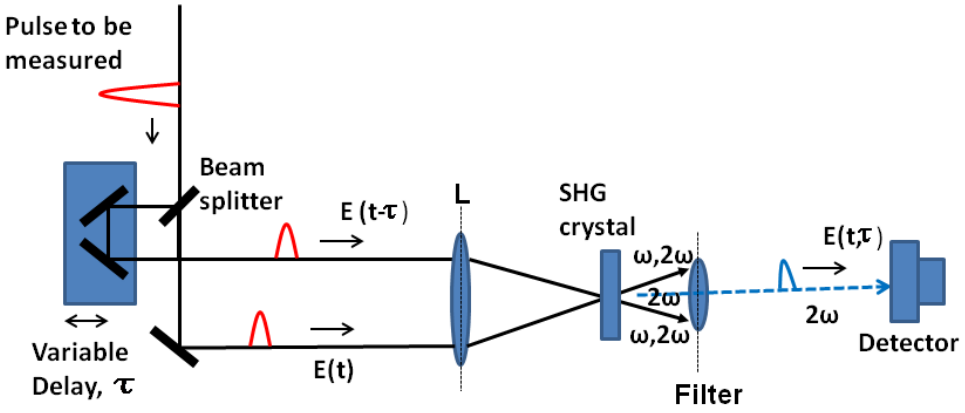

FIG. 3.2. Background free autocorrelation setup [26].

which excludes phase information. The pulse to be measured is split into two equal pulses $E(t)$ and $E(t-\tau)$ by a $50:50$ beam splitter. One of the pulses is delayed with respect to the other by the variable time, τ, by means of a translation stage. The one pulse is also translated such that after the two pulses reflect of the beam splitter for the second time, they are no longer collinear but parallel. These two pulses are then focused by a lens L and overlapped in a non-linear (NL) crystal (β-BBO). If the two pulses follow the same path length, then after the BBO crystal, a three beam pattern is observed as illustrated in FIG. 3.2. The one in the middle is only composed of the second harmonic frequency 2ω, while the other two beams contain both the fundamental frequency ω as well as the second harmonic, 2ω. The second harmonic signal in the center is only visible when the two pulse from the two arms of the autocorrelator have travelled the same path length and overlap in space and time. The second harmonic signal strength is a measure of the degree of overlap. Furthermore, as can be seen, the signal is generated in a direction that differs from either of the two beams generating the second harmonic light. This is due to momentum conservation.

To eliminate scattered fundamental light reaching the detector, a Schott glass filter (BG39)

is used to select only the second harmonic light and an aperture is used to block the two original beams (containing both the fundamental and second harmonic frequencies). Finally, the signal S(τ) is detected by a silicon photodiode detector and displayed on an oscilloscope.

3.2.2 Interferometric autocorrelation

The interferometric autocorrelator in FIG. 3.3 is a setup to generate signals which obey Equation (2.67). This setup can be described as follows: the incoming beam is split into

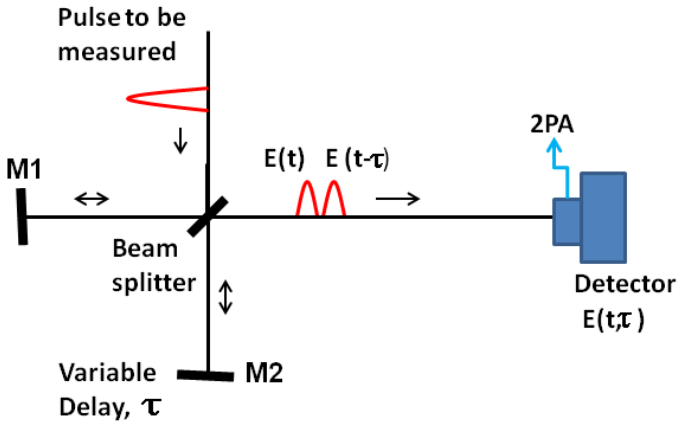

FIG. 3.3. Schematic diagram of the interferometric autocorrelator [26].

two beams with equal energy by a 50 : 50 dielectric beam splitter placed at 45°. Both beams $E(t)$ and $E(t-\tau)$ are reflected back by the mirrors M1 and M2 respectively. The delay between the two pulses, τ, is introduced by the translating mirror M2. The two replicas $E(t)$ and $E(t-\tau)$ are separated by τ, defined as the ratio of the difference in path length (δx) travelled by the two pulses and the speed of light c ($\tau = \frac{\delta x}{c}$). The pulses propagate collinearly in space and are focused onto a AlGaAs photodiode (2PA). The bandgap of AlGaAs is such that the photon energy of the laser pulses is to low to excite charge carriers into the conduction band. Two photons are necessary and hence only two-photon absorption is present. This is important since two-photon absorption is dependent on the square of the incident intensity, and hence when the two pulses overlap at the detector, an enhanced signal is detected. This signal is monitored by an oscilloscope.

From theory, we expect a peak to background ratio of 8 : 1. Achieving this is a good indication of the correctness of the measurement.

3.2.3 Pulse shaping autocorrelation and amplitude modulation

The procedure to correctly setup and align the $4f$-pulse shaper is outlined in the next section (section 3.3). This subsection will rather focus on the procedure for using the $4f$-pulse shaper in various experiments.

The $4f$ pulse shaper depicted in FIG 3.4, can be used as an autocorrelator. This has

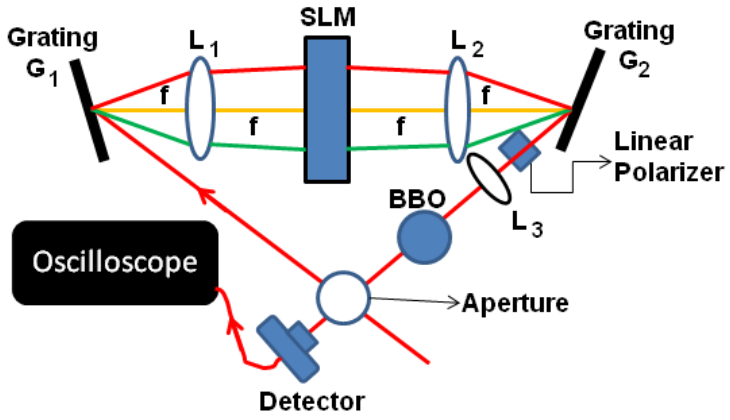

FIG. 3.4. Schematic diagram of the $4f$ pulse shaper autocorrelation setup used for the characterization of the pulse in the study.

the advantage that the autocorrelation measurement can be performed at the position of the proposed experiment. The basic layout of the $4f$-pulse shaper is as follows. The incident beam passes through an aperture, used for alignment purposes, before falling on the first of two gratings. Both gratings used in the setup are holographic gratings with a groove spacing of 1800 lines per millimeter. The first grating disperses the broadband incident beam, sending each frequency component in a different direction. The diffracted light then passes through a cylindrical lens. This lens collimates the beam, producing a parallel beam of spatially separated frequencies. The beam passes through the computer controlled liquid crystal spatial light modulator (SLM) (Jenoptik, SLM-640d) at the back focal plane of L_1. The SLM is a pixilated device that has the ability to change both

the amplitude (in conjunction with a polarizer at the output of the $4f$-shaper) and the phase of the individual frequency components falling on each of the individual pixels. The spectrum from the laser is essentially divided into 640 components which can each be manipulated independently. The beam then passes to the next cylindrical lens which focuses the modulated spectral components onto the second grating. The second grating recombines all the spectral components into a single beam before it passes through a Glan-Taylor polarizer. The polarizer, in combination with the SLM results in amplitude modulation.

In order to use the 4f-shaper to perform an autocorrelation measurement, the output from the $4f$-shaper is focused into a nonlinear crystal (β-BBO) by a 20 cm focal length lens. The SLM is used to produce two exact copies of the original pulse and to scan them in time across each other. This is done by applying a sinusoidal transfer function, see Equation (2.71). By varying the period of the sinusoid function, it is possible to scan the two pulses across each other in time. This is similar to what was done mechanically during the interferometric autocorrelation measurement. The second harmonic signal produced in the BBO is then again dependent on the relative delay between the two pulses. The signal, after being filtered from the fundamental by a suitable filter (Schott BG39), is detected by a photodiode and displayed on an oscilloscope.

The $4f$ pulse shaper was also used to obtain amplitude modulated pulses. Two examples, based on Equations (4.3) and (4.5), respectively, were demonstrated. The exact same setup was used, except that the nonlinear crystal and photodiode were replaced by a spectrometer (Aventes AvaSpec 3648). With this setup, the periodic amplitude modulation and central frequency blocking transfer function could be investigated.

3.3 The alignment of the $4f$-pulse shaper

The beam enters the system and hits the first grating at an incident angle i (angle between the grating normal and the incident beam (see FIG. 3.5)). The incident beam is dispersed (diffracted) by the grating before being collimated by the first lens in the $4f$ shaper. The grating needs to be orientated such that the diffracted beam is nearly the size of the SLM array when it reached the first lens. The amount of spreading can be controlled be changing

the incident angle, i. This can be done by rotating the grating. The functioning of the grating is discussed in depth in the next section.

3.3.1 Optical grating

The reflection grating is an optical element consisting of a highly reflective coating with many closely spaced parallel grooves. It is used to separate an incident beam into its constituent wavelength components, by diffracting the different components into separate angular directions.

A grating typically diffracts light into different diffraction orders. In general (this depends on the blaze of the grating) the first order is the most intense of the diffracted orders. This is the reason for choosing the first order ($m = 1$) during the setup of this experiment. Diffraction gratings are popularly used as dispersive elements since they are easy to use and the induced dispersion can be controlled geometrically. The specific gratings used in the setup are holographic reflection grating with 1800 lines/mm. In FIG. 3.5, a particular example is given where the incoming light consists of three different wavelengths incident at an incident angle i, which are then subsequently diffracted into three different directions at angles γ, θ and α from the normal to the grating surface. In the $4f$ setup used in the experiments, the diffraction gratings are used close to the Littrow angle, where the incident angle is close to the diffraction angle ($i \approx \theta$). This means that the diffracted beam propagates back in the direction of the incident beam [9].

Light diffracted from a grating will be observed at angles where the conditions for constructive interference are satisfied. This essentially means that the difference in path length, $\triangle\delta$, for two rays, originating from different spots on the grating, must be exactly a multiple of the wavelength. In terms of the groove spacing, d, this can be written as

$$\triangle\delta = d(\sin i + \sin\theta) = m\lambda, \tag{3.1}$$

where m is the diffraction order and λ is the wavelength.

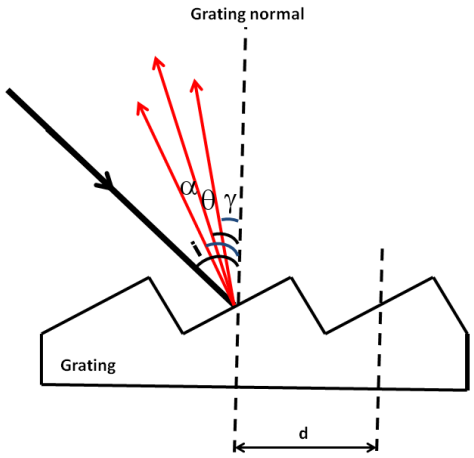

FIG. 3.5. Illustration of light incident on a grating close to Littrow angle.

3.3.2 Optimization of incident grating angle i

The incident angle of the grating has to be optimized for the bandwidth of the specific laser used in the experiment and the focal length of the lenses used in the setup. In order to determine the correct incident angle of the grating for our specific setup, let us consider three distinct wavelengths in our incident beam. The wavelengths are chosen such that two are on the edges of our incident spectrum and one is in the center. The wavelengths under consideration are $\lambda_1 = 773$ nm corresponding to the first ray at angle γ, $\lambda_0 = 800$ nm, the central ray at angle θ from the normal of the grating and $\lambda_2 = 827$ nm the third ray diffracted at angle α as shown in FIG. 3.6.

The three rays form a pattern on the lens of the size $L(i)$. The size $L(i)$ can be determined by considering the triangles jhk and jhg with respective rays λ_1 and λ_0 separated by the angle ω and λ_0 and λ_2 separated by the angle β, we may write

$$a = f \tan(\omega), \tag{3.2}$$

and

$$b = f \tan(\beta), \tag{3.3}$$

where a and b are the distance between two consecutive rays and f the focal length. The

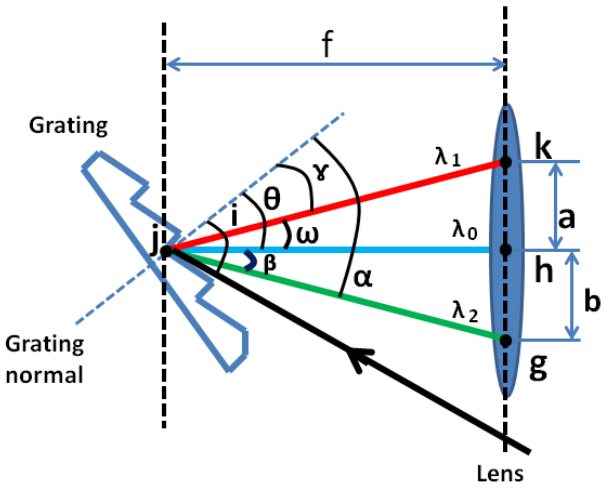

FIG. 3.6. Schematic diagram showing the size (or diameter) of the diffracting beam pattern on the lens.

angle ω and β depended on the diffraction angles γ, θ and α which are expressed as

$$\omega = \theta - \gamma, \tag{3.4}$$

and

$$\beta = \alpha - \theta. \tag{3.5}$$

From Equation (3.1), θ, γ and α are expressed as

$$\theta = \arcsin\left(\frac{m\lambda_0}{d} - \sin(i)\right) \tag{3.6}$$

for the central wavelength, then

$$\gamma = \arcsin\left(\frac{m\lambda_1}{d} - \sin(i)\right), \tag{3.7}$$

and

$$\alpha = \arcsin\left(\frac{m\lambda_2}{d} - \sin(i)\right), \tag{3.8}$$

for the extreme wavelengths. Substituting Equations (3.4), (3.6) and (3.7) into (3.2) and Equations (3.5), (3.6) and (3.8) into (3.3) leads to

$$a(i) = f\tan\left[\arcsin\left(\frac{m\lambda_0}{d} - \sin i\right) - \arcsin\left(\frac{m\lambda_1}{d} - \sin i\right)\right],$$

$$b(i) = f \tan\left[\arcsin\left(\frac{m\lambda_0}{d} - \sin i\right) - \arcsin\left(\frac{m\lambda_2}{d} - \sin i\right)\right].$$

The size of the pattern $L(i)$ is obtained as the difference between $a(i)$ and $b(i)$, given by

$$L(i) = a(i) - b(i) \tag{3.9}$$

The Equation (3.9) is a function of the incident angle i. The angle contributes to the orientation of the diffraction of light onto the lens. The beam size $L(i)$ has been simulated as illustrated in FIG. 3.7 to determine the correct incident angle i.

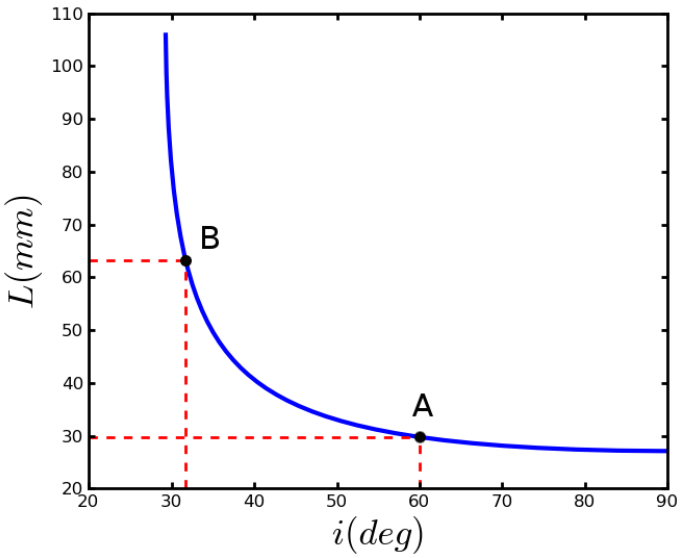

FIG. 3.7. The graph shows the dependence of the beam size at the first lens on the incident angle on the grating. Point A is for an incident angle of 60° and point B for an incident angle of 31.67°.

Due to layout consideration on the optical table, the $4f$ pulse shaper was initially setup with an incident angle of 60° on the first grating. This yielded a beam size of 29.5 mm on the LC-SLM. This result is the same as the one obtained with the theoretical calculations for the point A in FIG 3.7. However, it is important to note that our LC-SLM has a length of 64 mm. With this in mind, one can see that the 29.5 mm beam will cover less than half the number of pixels of the LC-SLM. The setup was then redesigned and based on the theoretical calculations, an incident angle of 31.5° was decided upon. This corresponds to point B in FIG. 3.7 and a beam size of 63 mm on the SLM. This implies that nearly 90%

of the LC-SLM is covered and any beam clipping is prevented.

For all the experiments to follow, an incident angle of $I = 31.5°$ on the first grating was used. The next step was to align the two lenses on the optical axis of the $4f$ pulse shaper. This was done with the aid of the Avantes AvaSpec-3648 fiber-coupled spectrometer, shown in FIG. 3.8. The optical axis of the $4f$-pulse shaper setup is determined by the incident

FIG. 3.8. Avantes AvaSpec-3648 spectrometer.

angle and orientation of the first grating. It corresponds to the path travelled by the central wavelength in our broad spectrum pulse, namely 800 nm. Without any lenses, the fiber connected to the spectrometer was placed in the far field such that the central wavelength (800 nm) enters the fiber. The first lens was then placed at its correct position, in such a way that the spectrum captured by the spectrometer did not change, followed by the second lens. This implied that the central wavelength (800 nm) passed through the center of both the lenses and that the lenses are properly aligned.

The distances between all the components were optimized by focusing the output from the $4f$-pulse shaper into a nonlinear crystal (β-BBO) and monitoring the generated second harmonic signal as a function of optical component position. When all the optical components are at their optimum position, the $4f$-pulse shaper should correspond to a zero pulse stretcher and hence the output pulse should have the shortest pulse length and produce the largest second harmonic signal.

As represented in FIG. 3.6, each ray is located at a fixed position on the LC-SLM. The curves shown in FIG. 3.9 were derived from the beam pattern ($L(i)$) Equation (3.9), but this time by considering the LC-SLM position $X(\lambda)$ as a function of wavelength. The plot in FIG. 3.9(a) shows the position on the SLM as a function of wavelength. The next

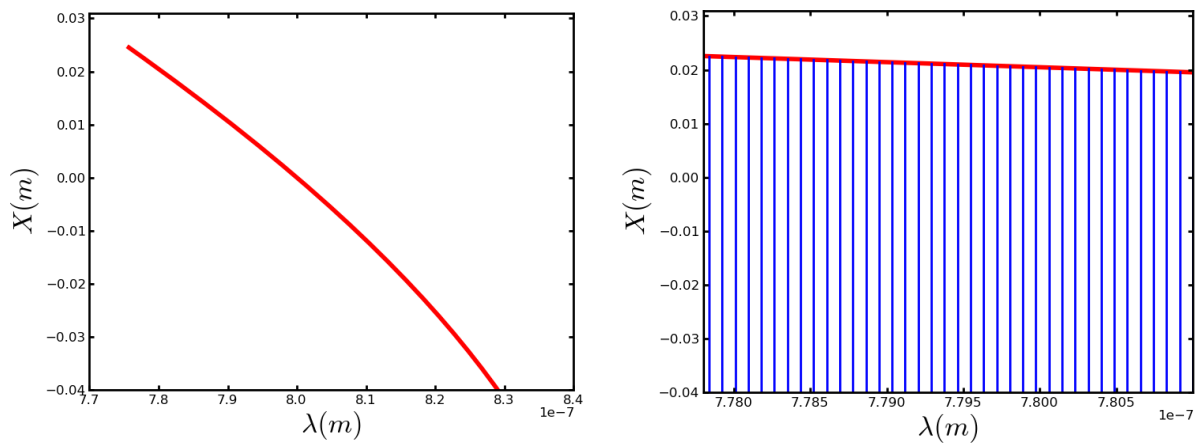

(a) (b)

FIG. 3.9. Spatial distribution of the wavelength on the SLM (a) and (b) when zoomed in.

FIG. 3.9(b) on the right was zoomed in to show how a pixel corresponds to an interval of wavelengths. These intervals are uniformly distributed and they are obtained by making the difference between the maximum and minimum wavelength values of the range divisible by the number of pixels.

Chapter 4

Results and Discussion

In this chapter, the numerical simulations and experimental results are presented and discussed. Section 4.1 shows the results of the numerical investigation of the Fourier transformations of various laser pulses. In section 4.2, the $4f$ pulse shaper is modeled using Fourier optics. Three examples of transfer functions have been investigated and the simulation results are presented in section 4.3. Lastly, section 4.4 describes all the experimental results in our study.

4.1 Numerical study of the Fourier transform

The results shown in this section are the numerical equivalent of the analytical results discussed in chapter 2. This is done by performing a numerical Fourier transform (a Fast Fourier Transform (FFT)) on the incident optical pulse which has now been represented numerically. An FFT is a computational method that has numerous applications in signal analysis [7]. In order to be able to trust the results obtained in section 4.3, it is necessary to test the computer algorithm employed that performs the FFT. To test this, data in the time domain, $E(t)$, was transformed to the frequency domain, $E(\omega)$, by means of an FFT, before being transformed back into the time domain, $E'(t)$, by means of an inverse FFT. The resultant signal was then compared to the original for consistency.

4.1.1 The electric field of a single Gaussian pulse

The data used in this study is an ultra-short Gaussian pulse, expressed as [10]

$$E(t) = \frac{1}{\sqrt{\sigma}} \left(\frac{2}{\pi}\right)^{\frac{1}{4}} \exp\left(-2\log(2)\left(\frac{t}{\sigma}\right)^2\right) \exp(iw_0 t). \tag{4.1}$$

The $2\log(2)$ term is introduced such that σ describes the full-width-at-half-maximum (FWHM) of the pulse, which is slightly different from the definition used in Equation (2.31). This electric field in the time domain is now converted to the frequency domain by means of an FFT.

$$E(\omega) = fftshift(fft(E(t))).$$

fftshift rearranges the output from fft by moving the zero-frequency component to the center of the array. In this specific case, it entails swiping the left half of the data array with the right half. The intensity of the pulse $I(\omega)$ is given by Equation (2.42)

$$I(\omega) = |E(\omega)|^2.$$

The electric field in the time domain is now again obtained by performing and inverse FFT on $E(\omega)$

$$E'(t) = ifft(E(\omega)).$$

The three functions $E(t)$, $I(\omega)$ and $E'(t)$ are graphically represented in FIG. 4.1. The same parameter values as in TABLE. 2.1 were used in the simulations.

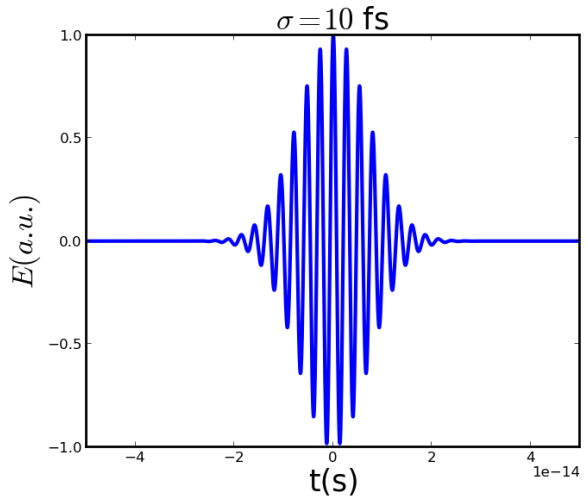

(a) Original field for $\sigma = 10$ fs.

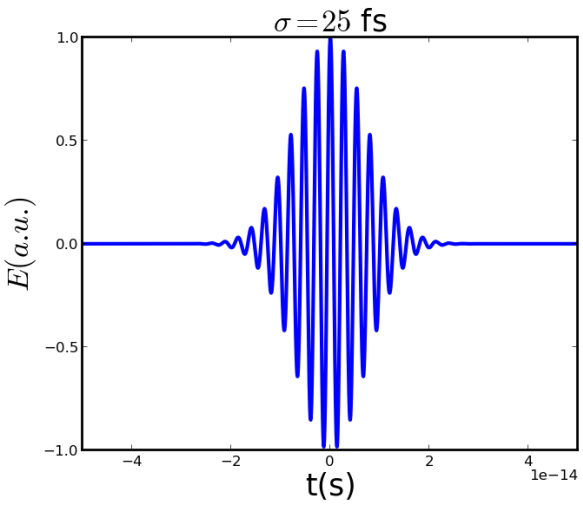

(b) Original field for $\sigma = 25$ fs.

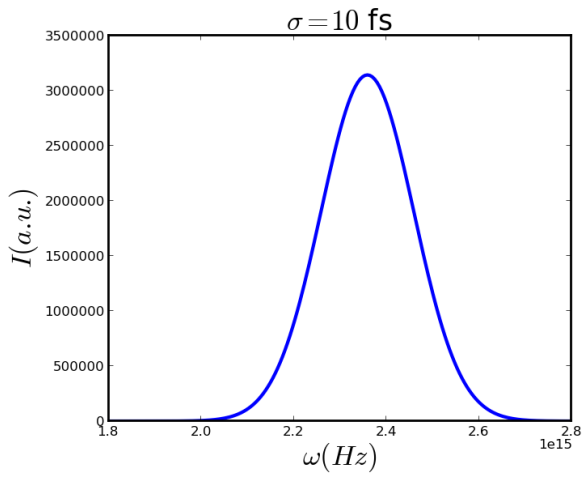

(c) Field $E(\omega)$ intensity for $\sigma = 10$ fs.

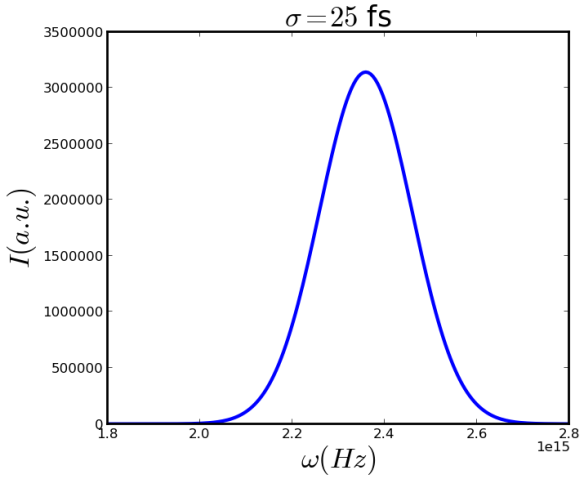

(d) Field $E(\omega)$ intensity for $\sigma = 25$ fs.

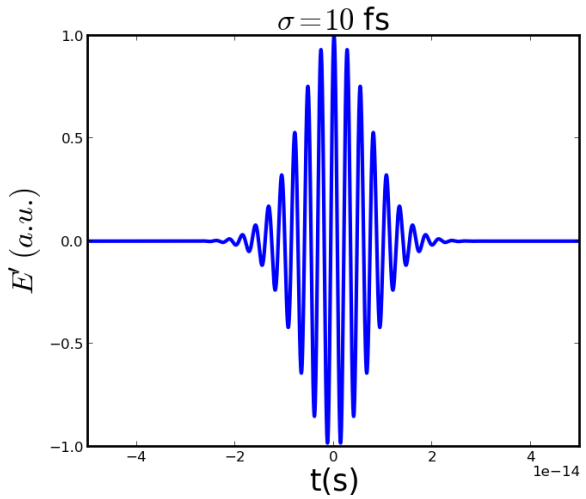

(e) Inverse FFT of $E(\omega)$ for $\sigma = 10$ fs.

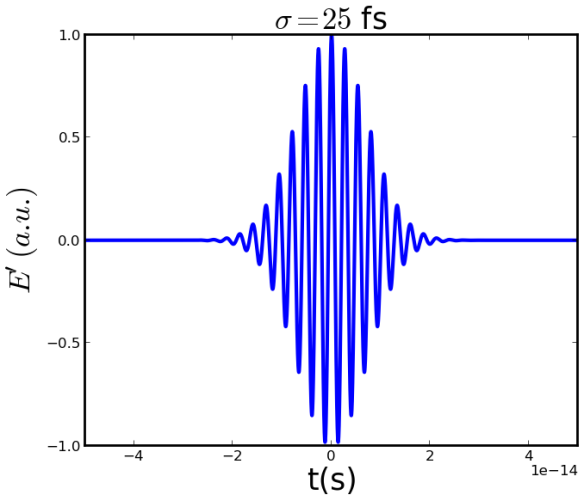

(f) Inverse FFT of $E(\omega)$ for $\sigma = 25$ fs.

FIG. 4.1. Numerical FFT simulations of temporal Gaussian pulses.

4.1.2 Electric field of two Gaussian pulses

The electric field of two ultra-short Gaussian pulses, separated by a time $T = 2\tau$ (with $\tau = 150$ fs), is given by

$$\begin{aligned} E(t) = &\frac{1}{\sqrt{\sigma}}\left(\frac{2}{\pi}\right)^{\frac{1}{4}} \exp\left(-2\log(2)\left(\frac{(t-\tau)}{\sigma}\right)^2\right)\exp(iw_0(t-\tau)) \\ &+\frac{1}{\sqrt{\sigma}}\left(\frac{2}{\pi}\right)^{\frac{1}{4}} \exp\left(-2\log(2)\left(\frac{t+\tau}{\sigma}\right)^2\right)\exp(iw_0(t+\tau)). \end{aligned} \tag{4.2}$$

It needs to be noted that $E(\omega)$, the FFT of $E(t)$, is a function with a Gaussian envelope but rapidly varying oscillations underneath. These oscillations are a result of the finite temporal domain as well as the sampling frequency of the time domain electric field data. To eliminate confusion which can result from this mathematical artefact, the intensity, rather than the electric field, is plotted in FIG. 4.2. It is worthwhile noting that the analytical curves shown in FIGs. 2.9, 2.10, 2.11 are very similar to those obtained numerically, depicted in FIG. 4.2.

4.2 Modeling of the $4f$ pulse shaper using Fourier optics

In order to model the propagation of the light through the $4f$ pulse shaper, we need to consider the spatial distribution of the light and the influence of each optical element on this spatial distribution. The process is done using the tools from Fourier optics. The theory of modeling each of the elements in the $4f$ pulse shaper was introduced in chapter 2. In this section, we numerically show the effect of the elements when light interacts with the element by simulating the interaction and examining the field intensity. For this analysis, we initially do not consider the SLM, and only look at the influence of the other optical components on the beam. The SLM is introduced in section 4.3.

FIG. 4.3 shows a schematic diagram of the modeling procedure. The vertical lines represent specific planes, before and after each element (free space is also considered an element). The functions, represented on the diagram, are summarized in TABLE 4.1.

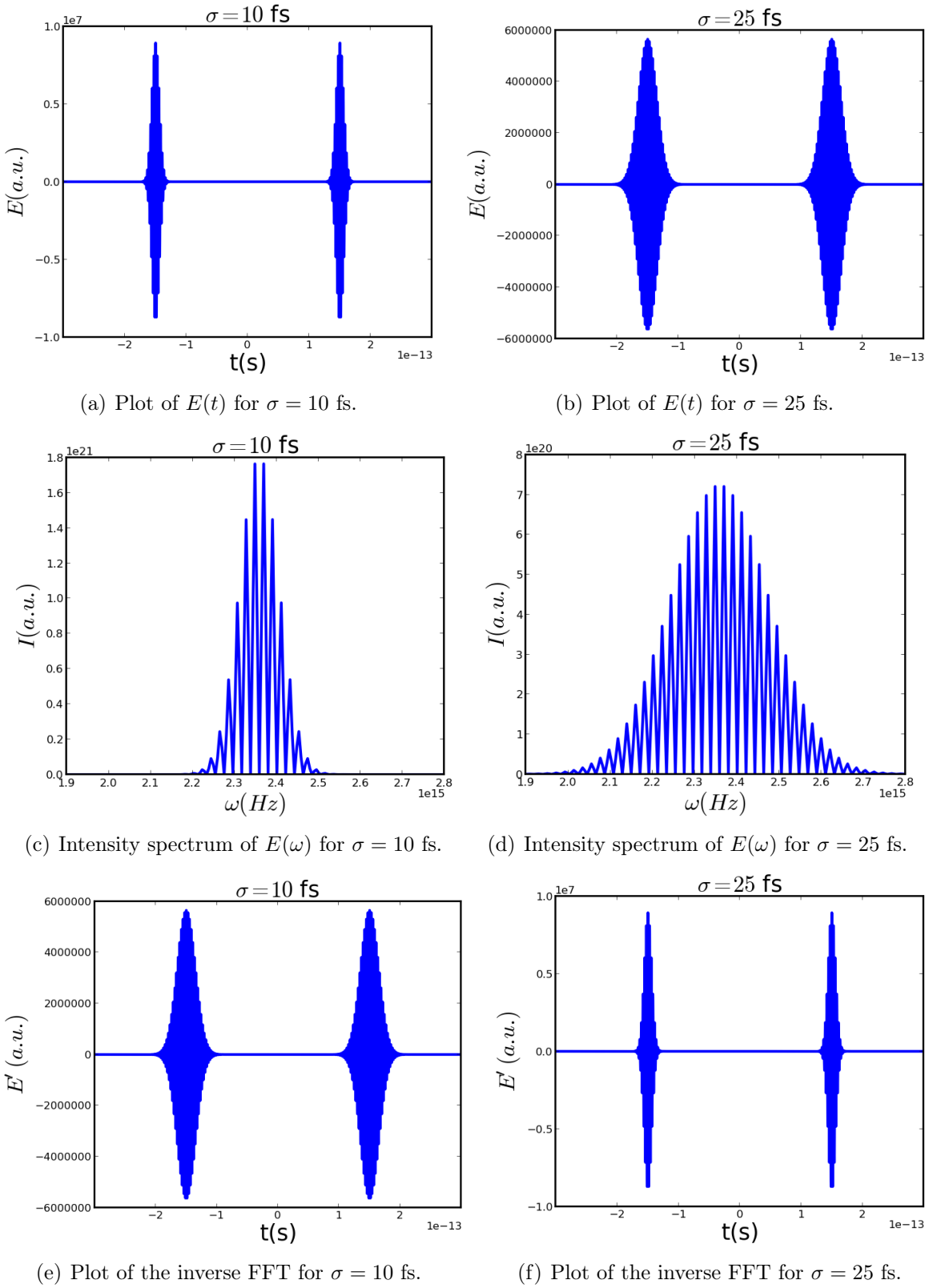

(a) Plot of $E(t)$ for $\sigma = 10$ fs.

(b) Plot of $E(t)$ for $\sigma = 25$ fs.

(c) Intensity spectrum of $E(\omega)$ for $\sigma = 10$ fs.

(d) Intensity spectrum of $E(\omega)$ for $\sigma = 25$ fs.

(e) Plot of the inverse FFT for $\sigma = 10$ fs.

(f) Plot of the inverse FFT for $\sigma = 25$ fs.

FIG. 4.2. Numerical FFT representations of two Gaussian temporal pulses separated by $T = 300$ fs.

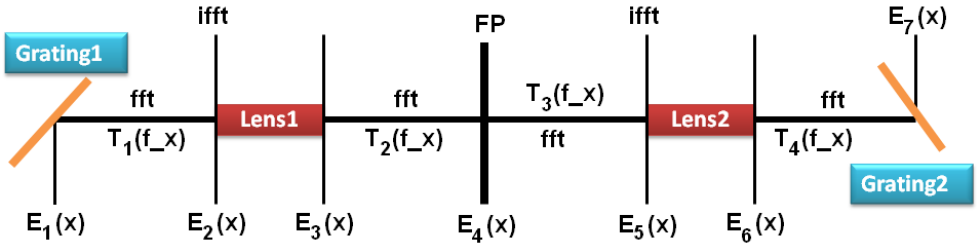

FIG. 4.3. Schematic showing the modeling procedure of the $4f$ system.

$E_1(x) = E_G(x)$ or $E_p(x)$
$T_1(f_x) = fft(E_1(x))H(f_x)$
$E_2(x) = ifft(T1(fx))$
$E_3(x) = E_2(x)U_l(x)$
$T_2(x) = fft(E_3(x))H(f_x)$
$E_4(x) = ifft(T_2(f_x))$
$T_3(f_x) = fft(E_4(x))H(f_x)$
$E_5(x) = ifft(T_3(f_x))$
$E_6(x) = E_5(x)U_l(x)$
$T_4(f_x) = fft(E_6(x))H(f_x)$
$E_7(x) = ifft(T_4(f_x))$

TABLE. 4.1. The functions that are used in the modeling of the 4f pulse shaper.

We only need to consider one dimension since all the optical elements used in the $4f$ pulse shaper only influence the beam in one dimension. Throughout all the investigations to follow, we will plot only the intensity distribution. The electric field contains phase information as well which is difficult to depict and is of lesser importance in this analysis.

4.2.1 Modeling the $4f$ system without gratings

Here we initially only consider the two lenses, i.e., the $4f$ pulse shaper without gratings and examine the intensity distribution at the end of the two lens system compared to the initial intensity distribution. We define the Gaussian beam as the initial field distribution $\mathrm{E}_1(x) = \mathrm{E}_G(x)$ described in Equation (2.58). Since we also have no dispersive elements in the setup, we consider a monochromatic wave with wavelength $\lambda_0 = 800$ nm. The initial intensity distribution is shown in FIG. 4.4(a).

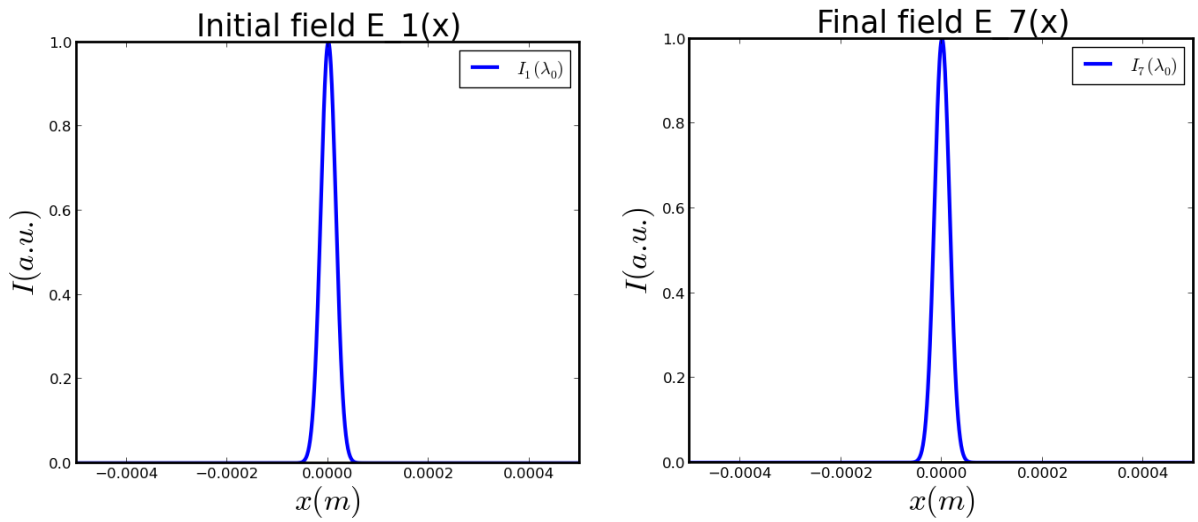

(a) Incoming signal $I_1(x)$.

(b) Outgoing signal $I_7(x)$.

FIG. 4.4. Intensity distributions of the beams with $\lambda_0 = 800$ nm.

The first step is to propagate the initial field $\mathrm{E}_G(x)$ a distance f. This is done by first Fourier transforming the electric field distribution to the spatial frequency domain where after it is multiplied by the free space propagation transfer function, $\mathrm{H}(f_x)$, described in Equation (2.59). This yields $\mathrm{T}_1(f_x)$. Since the lens acts in space, we then first need to perform an inverse Fourier transform on $\mathrm{T}_1(f_x)$ before multiplying it with the lens transfer function, $U_l(x)$, described in Equation (2.61). This inverse Fourier transform yields the field distribution, $\mathrm{E}_2(x)$, at a plane $z = f$ in front the first lens, as seen in FIG. 4.3. $\mathrm{E}_2(x)$ is then multiplied by $U_l(x)$ to obtain $\mathrm{E}_3(x)$, the field distribution just behind the first lens. In order to examine the effect of the lens on the electric field distribution, we plot the intensity before and after the lens. This can be seen in the left hand graph of FIG. 4.5(a). It should be clear from this graph that the lens has no effect on the beam shape or intensity. This is as expected since a lens only changes the phase of the beam. From here, we propagate the beam to the symmetry plane, FP. In order to do this, we need to first perform a Fourier transform on the beam, back into spatial frequency. The beam in spatial frequency is then again multiplied by the free-space propagator, $\mathrm{H}(f_x)$, to obtain $\mathrm{T}_2(f_x)$. The beam is now at the symmetry plane between the two lenses and the spatial distribution can again be obtained by performing an inverse Fourier transform. This yields the distribution $\mathrm{E}_4(x)$. This whole procedure as described is repeated with $\mathrm{E}_4(x)$ in the place of $\mathrm{E}_1(x)$ in order to propagate the beam to $\mathrm{E}_7(x)$.

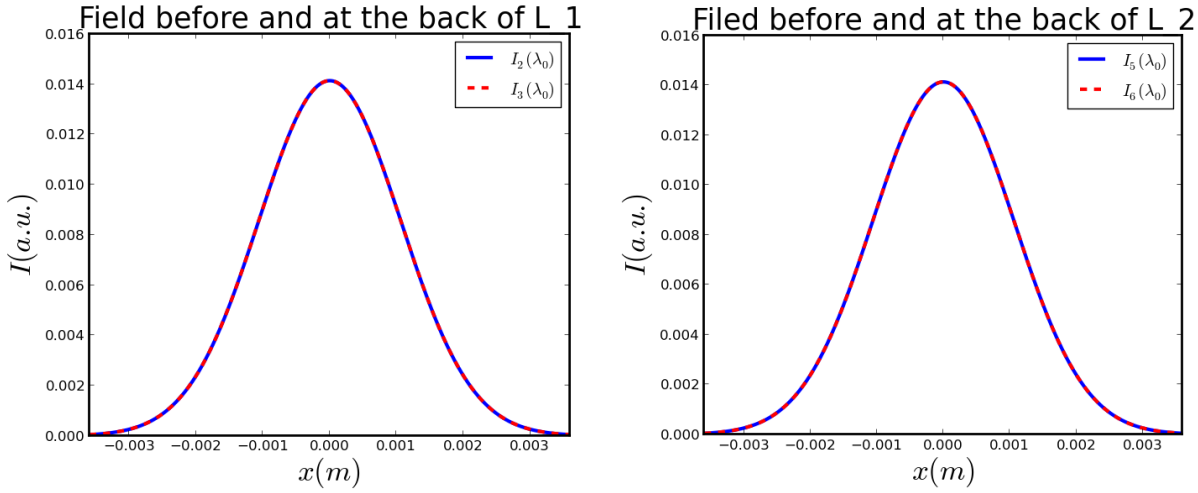

(a) (b)

FIG. 4.5. Intensity field distributions in front of and at the back of lenses L_1 (a) and L_2 (b).

The graph in FIG. 4.5(b) shows the intensity distribution of the field just in front and just behind the second lens. Again, the lens has no effect on the field distribution as can be expected. Furthermore, the two graphs in FIG. 4.5 look exactly the same, which again is as expected because of the inherent symmetry of the optical layout. When comparing the two graphs shown in FIG. 4.4, it is again clear the incident intensity distribution and the intensity distribution at the exit are exactly the same. This is again as expected for a $4f$ optical arrangement and proves that the setup does nothing to the intensity distribution.

4.2.2 Modeling the $4f$ pulse shaper with gratings

In this case, gratings are included in the $4f$ pulse shaper. Light is diffracted by the presence of the dispersive optical element into different rays. Three diffraction wavelengths have been considered for this study. Each wavelength is distinguished by the colours defined as: red (dashed lines) represents the maximum wavelength $\lambda_{max} = 850$ nm, green (hard lines) represents the central wavelength $\lambda_0 = 800$ nm and blue (dot-dashed lines) represents the minimum wavelength $\lambda_{min} = 750$ nm. The intensity distribution of the incoming $I_1(x)$ and the outgoing $I_7(x)$ beam at the grating planes are compared as shown in FIG. 4.6. The rays are still on top of one another on both grating planes G_1 and G_2 (see FIG. 2.13).

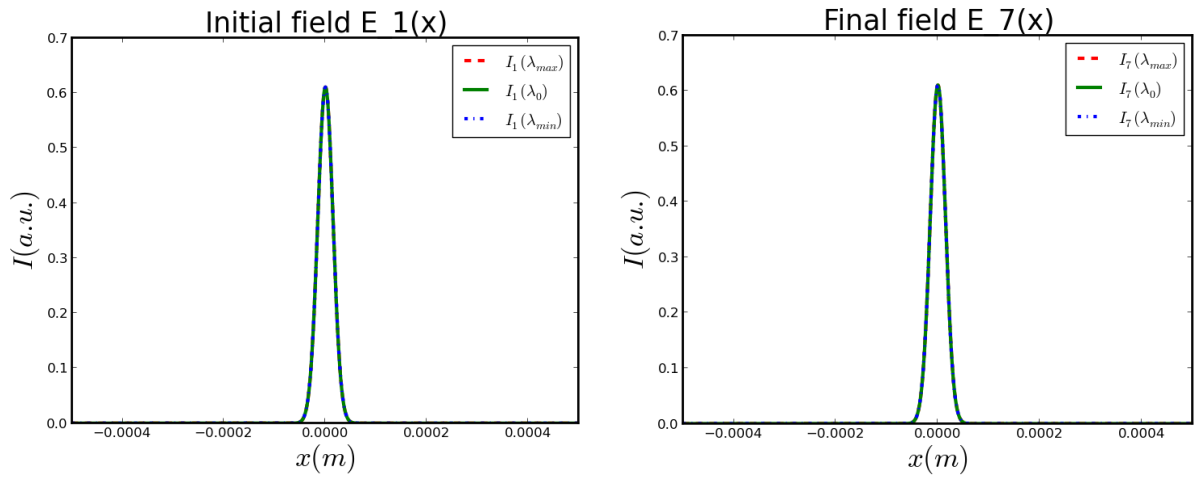

(a) (b)

FIG. 4.6. Simulations of the incoming $I_1(x)$ (a) and the outgoing $I_7(x)$ (b) intensities with $\lambda_{max} = 850$ nm, $\lambda_0 = 800$ nm and $\lambda_{min} = 750$ nm.

The first plot in FIG. 4.6(a) was obtained by applying the field $E_p(x)$ after the grating G_1 in Equation (2.64), which is considered as the incident field $E_1(x) = E_p(x)$ in this case. The path length of the field into the system can be described by first Fourier transforming the beam $E_p(x)$ in spatial frequency before it propagates the distance f. The FFT of $E_p(x)$ multiplied by the transfer function $H(f_x)$ of free space in Equation (2.59), gives $T_1(f_x)$. Therefore, at the plane $z = f$ in front of the first lens in FIG. 4.3, we evaluate the inverse Fourier transform of $T_1(f_x)$ which yields the field distribution $E_2(x)$. $E_2(x)$ is then multiplied by the transfer function of the lens in Equation (2.61) to obtain $E_3(x)$, the field distribution behind L_1. The effect of the lens on these fields can be investigated by plotting the intensity distributions ($I_2(x)$ and $I_3(x)$) as represented in FIG. 4.7(a).

Now we want to propagate the beam through the symmetry plane, FP between the two lenses. To accomplish that, we first apply the FFT to the field $E_3(x)$. The latter is multiplied by the free space function $H(f_x)$ to obtain $T_2(f_x)$. From here, we perform an inverse Fourier transform of $T_2(f_x)$ to get the field distribution $E_4(x)$ in space at the FP. As mentioned before, the whole procedure is again repeated with $E_4(x)$ in the place of $E_1(x)$ in order to propagate the beam to $E_7(x)$.

Since the wavelength is varying in space, each field has three distinct pulses at the planes of L_1 and L_2. All the fields in front of L_1 are denoted by $I_2(\lambda_{max})$, $I_2(\lambda_0)$ and $I_2(\lambda_{min})$ and

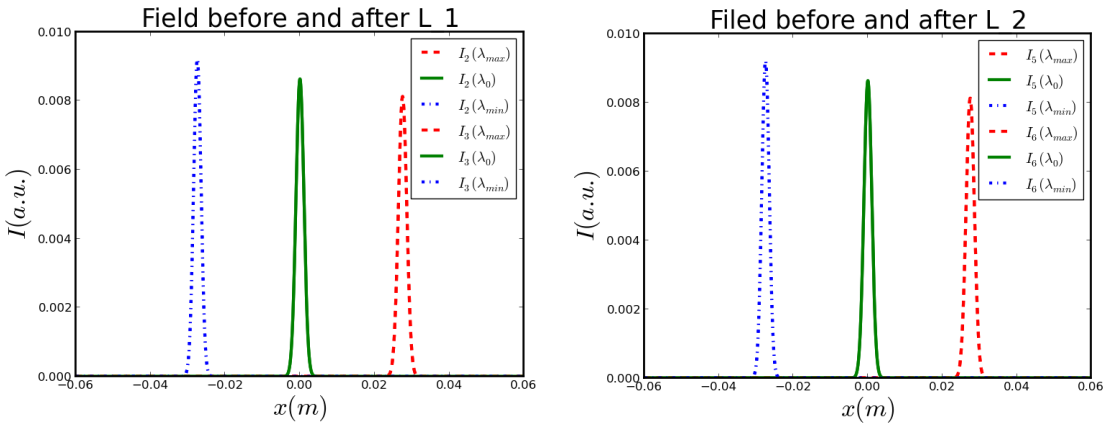

(a) (b)

FIG. 4.7. Intensity simulations at the planes of the lenses L_1 (a) and L_2 (b) in a $4f$ system with gratings.

those behind L_1 are denoted by $I_3(\lambda_{max})$, $I_3(\lambda_0)$ and $I_3(\lambda_{min})$. The same notation has been used at the planes of L_2. The simulation of the intensities at the planes of lenses L_1 and L_2 are respectively given in FIG. 4.7(a), (b). It is seen that the pulses are shifted and have different amplitudes. Again, the lens can only change the phase of the field not the shape and intensity. Comparing the incident and output intensity distributions in FIG. 4.6, it can be seen that they are exactly the same as expected. Again, the graphs in FIG. 4.7 are also similar.

4.3 Modeling of example Transfer Functions (TF) applied to the SLM in a $4f$ pulse shaper

In this section we consider the $4f$ pulse shaper with the SLM placed at the symmetry plane (FP in FIG. 4.3). We apply a few specific example transfer functions to the SLM and investigate the effect on the temporal profile of the laser pulse. As was shown in subsection 4.2.2, different frequency components are located at different positions at the FP plane. This implies that each element (pixel) of the SLM can address different frequencies. Even though the SLM can manipulate both the amplitude and phase of the individual frequency components, in these examples we will only consider amplitude modulation. As input for these simulations, we consider an ultra-short, broad bandwidth laser pulse, $E(t)$ described

by

$$E(t) = \frac{1}{\sqrt{\sigma}} \left(\frac{2}{\pi}\right)^{\frac{1}{4}} \exp\left(-2\log(2)\left(\frac{t}{\sigma}\right)^2\right) \exp(iw_0 t).$$

where $\omega_0 = \frac{2\pi c}{\lambda_0}$ is the central angular frequency and the pulse duration $\sigma = 25$ fs. By applying different transfer functions to the SLM the temporal shape of the output pulse can be manipulated. This manipulation can be arbitrary and depends on how the transfer function is defined. The following three subsections provide examples of such manipulation.

4.3.1 Central transfer function TF_c

Without loss of generality, central refers to the fact that the central frequencies in the pulse spectrum are blocked by the transfer function. The central transfer function TFc used in our simulations can be represented as:

$$TF_c = \underbrace{1, \ldots\ldots, 1}_{m}, \underbrace{0, \ldots 0}_{q=21}, \underbrace{1, \ldots\ldots 1}_{m}. \tag{4.3}$$

The number of points, n, in the range of TFc is given by

$$n = 2m + q, \tag{4.4}$$

where m is the number of elements equal to one and q is the number of elements equal to zero. The twenty-one zeros ($q = 21$) were selected such that 10 elements to the left of the central frequency and 10 to the right of the central frequency are zero. The zeros correspond to blocking the specific frequencies. FIG. 4.8(a) shows the electric field magnitude of the incident pulse before any modulation in frequency domain and FIG. 4.8(b) the transfer function that is to be applied. FIG. 4.9(a), shows the product of the electric field magnitude with the transfer function, $P(\omega)$, in frequency domain and FIG. 4.9(b) the resultant pulse in time domain after an inverse Fourier transform, $P'(t)$. As can be seen in FIG. 4.9(a), the central frequencies of the input pulse have been removed by the transfer function, TF_c. The rest of the frequency components in the input pulse are left unchanged. The resultant output pulse clearly displays a pulse train in the time domain. The pulses are symmetric around the central pulse and have decreasing amplitude. This

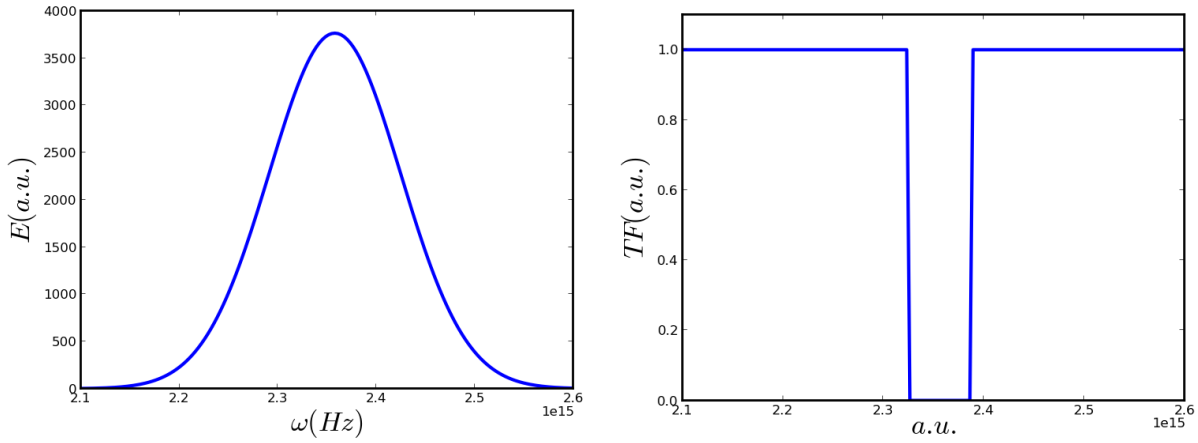

(a) (b)

FIG. 4.8. Plots for the input electric field $E(\omega)$ (a) and the central transfer function TF_c (b).

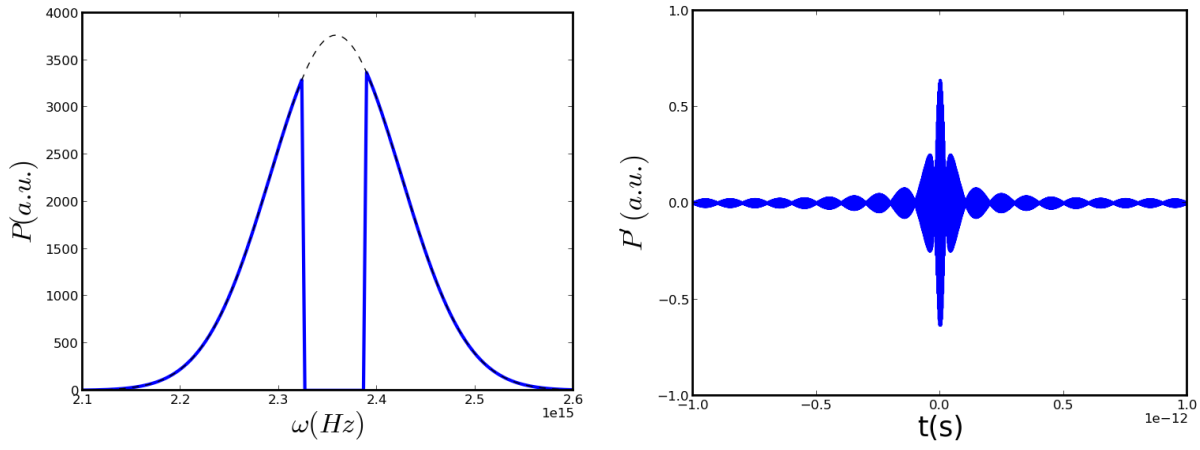

(a) (b)

FIG. 4.9. Simulation of the product $P(\omega)$ of the electric field $E(\omega)$ with the TF_c (a) and its inverse $P'(t)$ (b).

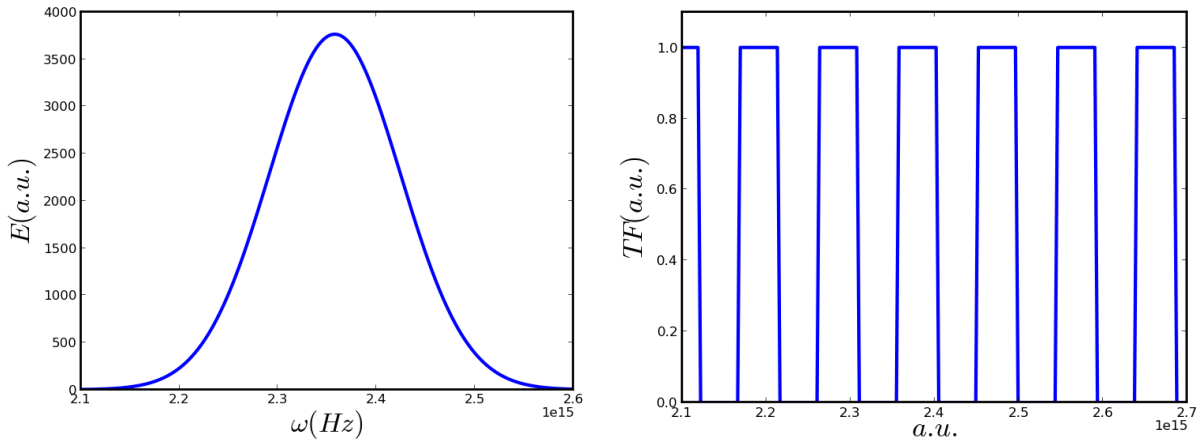

(a) (b)

FIG. 4.10. Simulations of the input electric field magnitude (a) and the periodic transfer function (b).

simulation clearly shows how amplitude modulation in the frequency domain can influence the pulse in the time domain.

4.3.2 Periodic transfer function TF_p

In this case, the transfer function TF_p, is defined as a periodic sequence of two elements, 1 (one) and 0 (zero). In this fashion it will periodically block different frequency components. It is represented as follows:

$$TF_p = \underbrace{1, ..., 1}_{15}, \underbrace{0, ..., 0}_{15}, \underbrace{1, ..., 1}_{15}, \underbrace{0, ..., 0}_{15}, ... \tag{4.5}$$

For this specific case, the sequence is split into groups of fifteen elements each as shown in Equation 4.5. In the simulations, we can arbitrarily choose to start with the group of ones followed by the zero elements group. The electric field magnitude in frequency domain, $E(\omega)$, is shown in FIG. 4.10(a) and the transfer function in FIG. 4.10(b), TF_p. FIG. 4.11(a) shows the product electric field, $E(\omega)$, with the transfer TF_p while on the right, the resultant pulse in the time domain is displayed, $P'(t)$, is shown in FIG. 4.11(b). As can be seen in the plot of $P'(t)$, the resultant pulse in the time domain consists of a sequence of well separated pulses with decreasing amplitude. The sequence of pulses is symmetric around the origin. The separation between the pulses is determined by the period of the

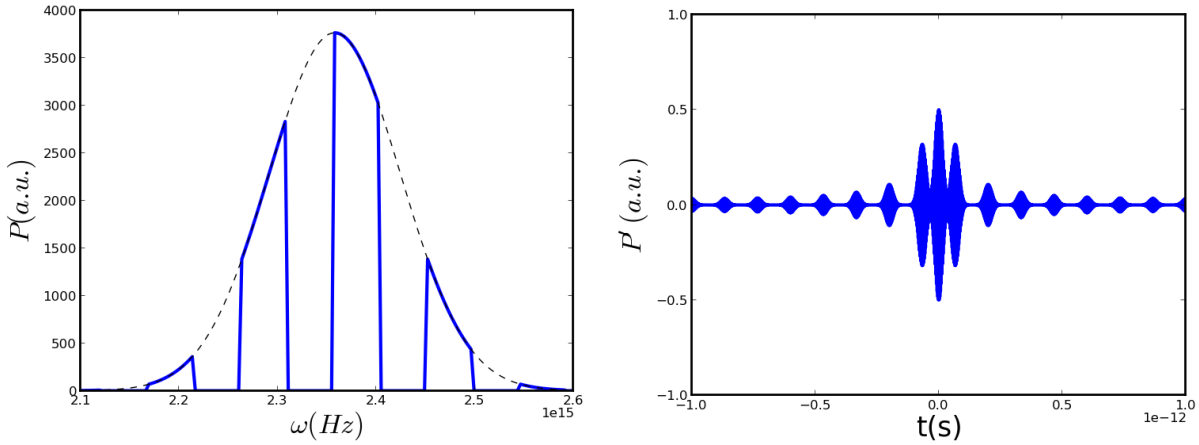

(a) (b)

FIG. 4.11. Simulations of the product $P(\omega)$ (a) and its inverse $P'(t)$ (b).

transfer function.

4.3.3 Sinusoidal transfer function TFs

In this section we investigate the sinusoidal transfer function (first introduced in Equation (2.71)) that is used in the pulse shaping autocorrelation measurement (subsection 4.4.4). FIG. 4.12(a) shows the incident electric field in the frequency domain, $E(\omega)$ and the sinusoidal transfer function TF$s(\omega, \tau)$ on the right (FIG. 4.12(b)). The product of the electric field magnitude $E(\omega)$ and TF$s(\omega, \tau)$ along with the resultant pulse in the time domain, $P'(t)$, are shown in FIG. 4.13(a), (b). The resultant pulses in the time domain are exact replicas of the original pulse separated in time by $\tau = 300$ fs (as was specified in the transfer function, TF$s(\omega, \tau)$). The only difference being that the amplitude of the electric field of each of the pulses is halved. For this simulation γ, in Equation (2.71), was set to 1.

4.4 Experimental results

This section contains the results of all experiments performed, as described in Chapter 3. They include results on the polarization control experiments, the three autocorrelation measurements and two examples of transfer functions applied to the SLM.

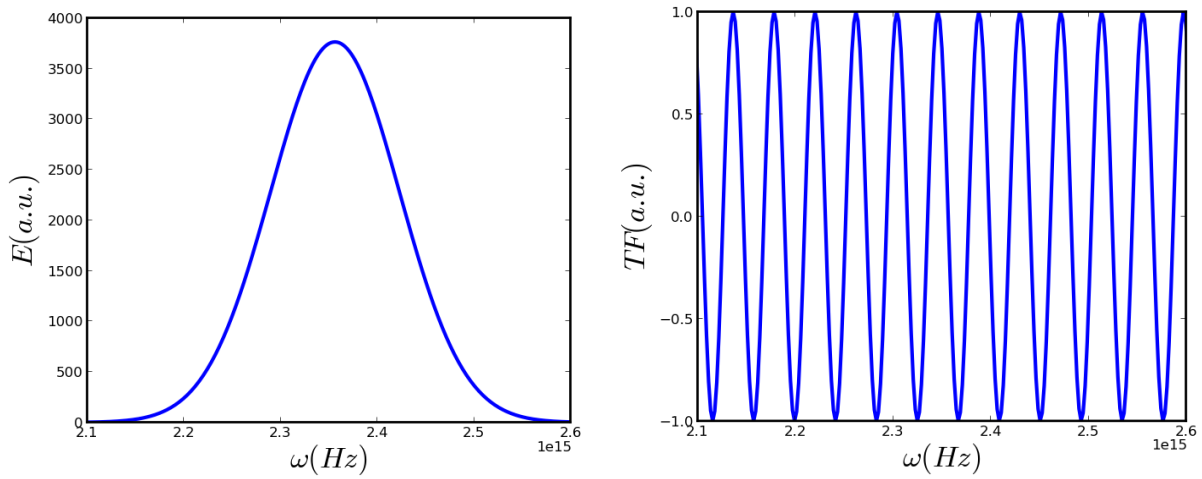

(a) (b)

FIG. 4.12. Simulations of $\tilde{E}(\omega)$ (a) and the sinusoidal TF$s(\omega, \tau)$ (b).

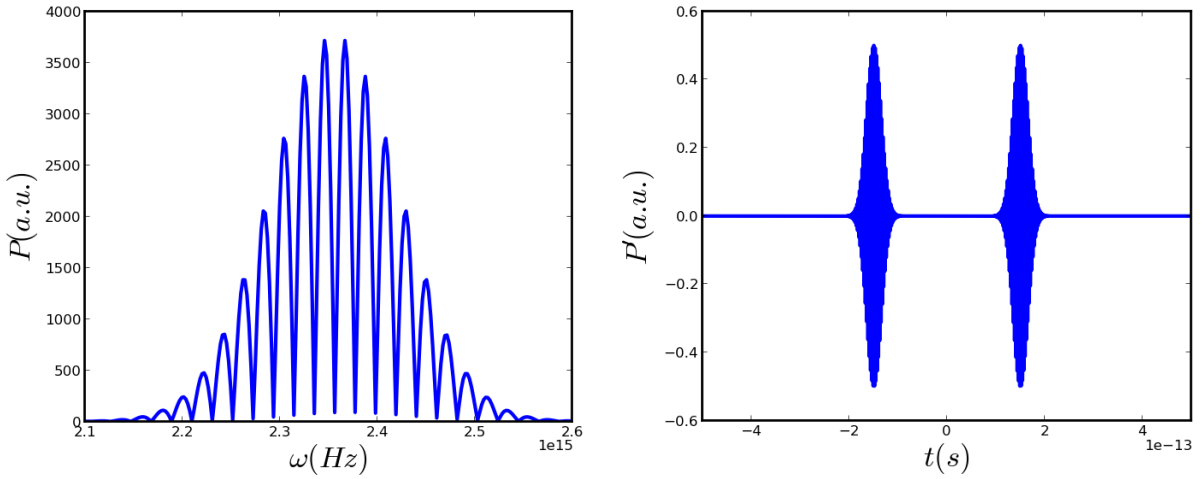

(a) (b)

FIG. 4.13. The product $P(\omega)$ of the electric field with the TF (a) and its inverse $P'(t)$ (b).

4.4.1 Polarizer

The experiment on polarization using the setup in FIG. 3.1 was performed in order to investigate the nature of polarized light. Three types of optics that influence the polarization have been used, namely a half-wave plate, a quarter-wave plate and a linear polarizer. A He-Ne laser with polarized output was used in this study and the polarizer was used as analyzer in order to observe the effect of the half-wave plate and the quarter-wave plate on the polarization of the beam.

4.4.1.1 Half-wave plate

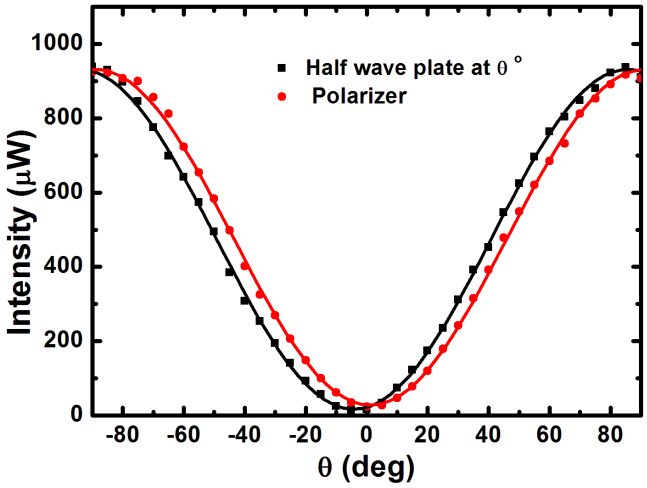

FIG. 4.14. Measurements of the power transmitted by the analyzer with a half-wave plate placed at 0°.

We first measured the power of the linear polarized beam transmitted by the polarizer. This was done by rotating the analyser clockwise from 0° to −90° and then, counterclockwise from 0° to 90°. The same procedure was used throughout the experiment when the wave plates were inserted in the experimental setup. A half-wave plate was added in front of the polarizer to investigate the polarization state of the incoming beam. The data obtained is plotted in FIG. 4.14. The dots represent the measurement without the half-wave plate inserted and the squares the measurement with the half-wave plate inserted. This was done by fixing a half-wave plate at $\theta = 0°$ and then rotating the analyser. FIG. 4.14 shows

that the graph of a half-wave plate is shifted by $-5°$ compared to that of the polarizer. As can be seen in FIG. 4.14, the half-wave plate does not influence the energy transmitted by the analyzer. From here, the half-wave plate was rotated through 30° and then 45° in

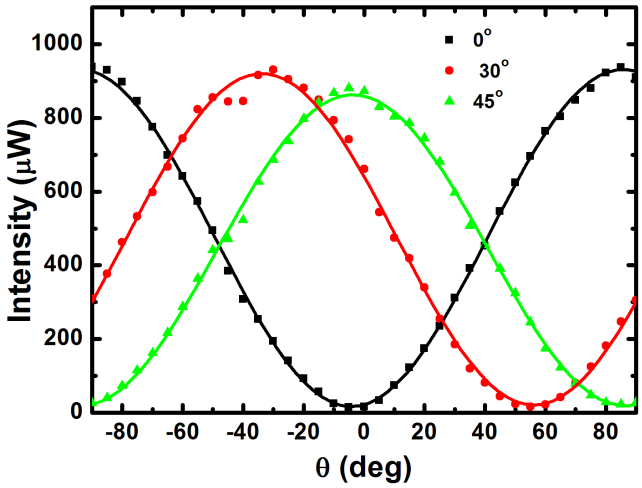

FIG. 4.15. Measurements of the transmitted power from the analyzer, with the half-wave plate placed at three different polarization angles 0°, 30° and 45°.

order to examine its effect on the transmitted beam as shown in FIG. 4.15. The graph of the transmitted field with the half-wave plate at 45° has been shifted by 90° compared to the one with the half-wave plate at 0°. That means the half-wave plate has rotated the polarization by twice the angle between the incident field and the half-wave plate axis.

4.4.1.2 Quarter-wave plate

The same experiment was performed but in this case, the half-wave plate was replaced by the quarter-wave plate. The graphs in FIG. 4.16 show the measurements of the output beam for the quarter-wave plate placed at $\theta = 0°$ and the polarizer.

As can be seen in FIG. 4.16 the quarter-wave plate-axis is shifted by 7.5° compared to that of the polarizer. This 7.5° shift means the beam passing through the quarter-wave plate is slightly elliptically polarized which results in a reduction in transmitted energy through the polarizer. The quarter-wave plate was then turned to 37.5° and 45° and the results are plotted in FIG. 4.17.

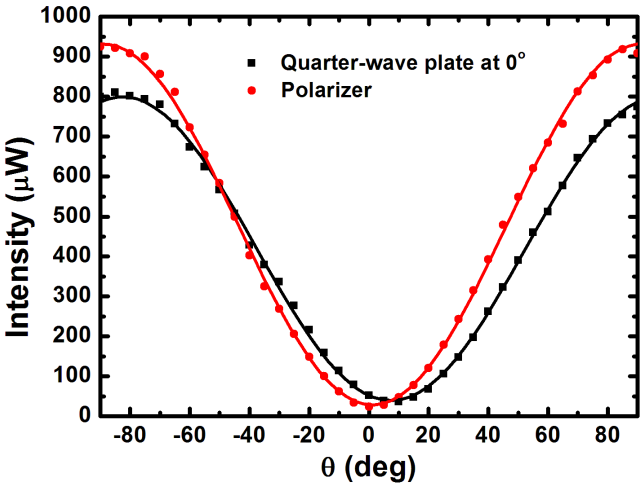

FIG. 4.16. Measurements of the irradiance transmitted by the polarizer with a quarter-wave plate placed at 0°.

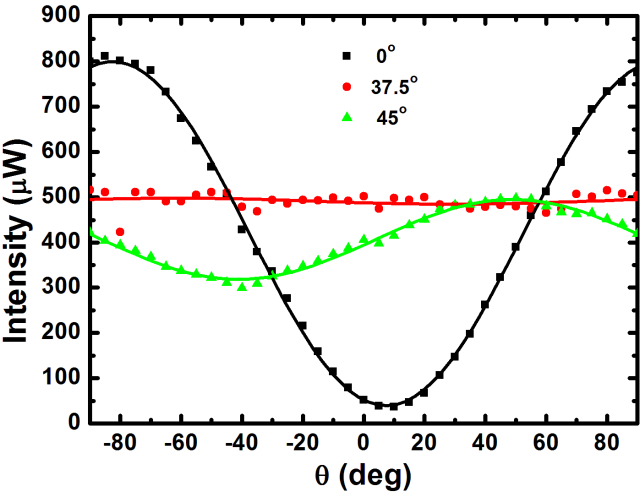

FIG. 4.17. Measurements of the output irradiance, with the quarter-wave plate placed at three different polarization angles 0°, 37.5° and 45°.

FIG. 4.17 shows the state of the output polarized light at three different positions of the quarter-wave plate. As one can see, at 37.5°, which would be 45° but for the initial shift, the transmitted power is constant. This indicates that light is circularly polarized. In addition, the power is reduced by half (taking errors into account).

All the Figures were fitted by using Malus's law Equation (2.14).

4.4.2 Background free autocorrelation

The aim of this experiment was to measure the pulse width of a femtosecond laser using a background free autocorrelator. This technique is used because of the simplicity of the setup and the extraction of the pulse width. The autocorrelation measurement was performed by moving the one arm of the autocorrelator by a constant velocity of $v = 0.01$ mm/s, thereby introducing a varying temporal delay between the two pulses.

As the two pulses are scanned across each other in a nonlinear crystal, the resultant second harmonic light is measured by a photodiode of which the output is displayed on an oscilloscope. The time duration of the overlap can therefore easily be measured on the oscilloscope and was found to be 2 s. The pulse duration in space can then be obtained by the simple relation, $D = 2tv$. The factor 2 comes into the Equation because the effective speed of the translation stage is doubled when one considers the change in optical path length. The pulse length is measured at full-width-at-half-maximum. The temporal width of the autocorrelation signal is then simply $\tau_{AC} = \frac{D}{c} = 133$ fs. The actual pulse duration is related to τ_{AC} by a factor of square-root of 2 and is given by

$$\sigma = \frac{\tau_{AC}}{\sqrt{2}}. \tag{4.6}$$

The result obtained in this experiment is shown in FIG. 4.18. The measurement gives a time duration of $\sigma = 94$ fs. Only the envelope of the autocorrelation signal is measured because of the non-collinear experimental setup. This is also the reason for no background signal when the pulses do not overlap.

4.4.3 Interferometric autocorrelation

The next autocorrelation technique that was investigated was the interferometric autocorrelator. It is an analogue of the pulse shaper assisted autocorrelation, discussed in subsection 4.4.4. The setup uses a collinear arrangement and a two-photon detector to measure the signal. The output from the detector was visualized on an oscilloscope. The timescale on the oscilloscope is related to the movement of the translation stage (mirror mounted on an audio speaker) and not to the pulse length. This timescale needs to be converted before the pulse length can be measured. This is done by converting the time

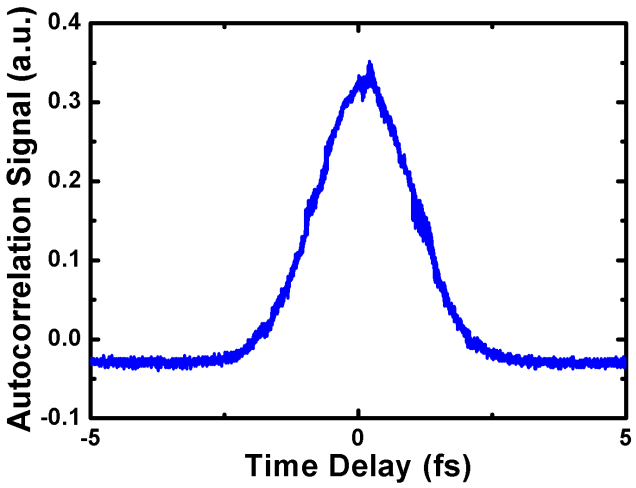

FIG. 4.18. Background-free autocorrelation measurement for a Gaussian laser pulse of pulse duration $\sigma = 94$ fs.

scale on the oscilloscope to fs by means of multiplication of the appropriate conversion factor. This conversion factor is calculated by considering the fact that the time between two consecutive fringes in the autocorrelation trace corresponds to the time taken for the light to travel one wavelength (central wavelength 800 nm). This is illustrated in the zoomed graph of FIG. 4.19.

The autocorrelation full-width-at-half-maximum (FWHM) is calculated by counting the number of fringes that lie above the half-maximum value and multiplying it by the time it took for light to travel between two fringes. The FWHM of the autocorrelation trace was found to be 122 fs. This gives us a pulse duration of $\sigma = 86$ fs. An important quality of the interference autocorrelation trace is the peak to background ratio. This can be understood as follows:

- At points a and b, the pulses are not overlapping, which means that $A^{(2)}_{IA}(\tau) = 2\int_{-\infty}^{+\infty} E^4(t)dt$ at $\tau = \infty$. This portion is called Background.
- At the maximum peak of the signal (point o) the pulses are completely overlapping, implying that the fields are in phase and leading to the constructive interference with the maximum value of $A^{(2)}_{IA}(\tau) = 16\int_{-\infty}^{+\infty} E^4(t)dt$ when the delay is $\tau = 0$.
- At the minimum point e, the fields are out of phase. The resultant field is zero, i.e.,

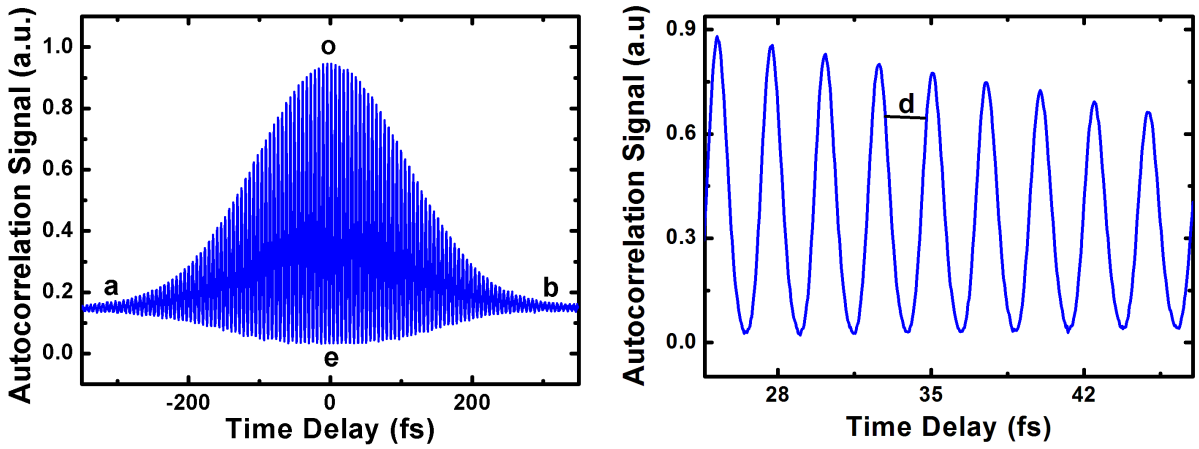

(a) (b)

FIG. 4.19. An interferometric autocorrelator measurement showing a pulse with duration 86 fs (a) and when zoomed in (b).

there is no field, thus leading to the destructive interference.

4.4.4 Pulse shaper autocorrelation

This measurement was done by using the $4f$-pulse shaper, described in detail in subsection 3.2.3. A double pulse is created by applying a sinusoidal transfer function to the SLM. The function is described in Equation 2.71. These two pulses are then scanned across each other by varying the frequency of the sinusoidal transfer function. Two measurements were performed with the aim of showing the versatility and power of the pulse shaping technique.

In the first measurement (FIG. 4.20) we shifted the carrier phase together with the envelope by setting $\gamma = 1$. This corresponds to a interferometric autocorrelation measurement. In the second measurement (FIG. 4.21) we kept the carrier phase fixed and only shifted the envelope ($\gamma = 0$). This relates to an intensity autocorrelation measurement.

The generated second harmonic frequency was detected by a photodiode and displayed on an oscilloscope. The measurement was calibrated using the same procedure as was used for the interferometric autocorrelation, describe in subsection 4.4.3, namely by considering the time taken for light to have travelled one wavelength. This time corresponds to two

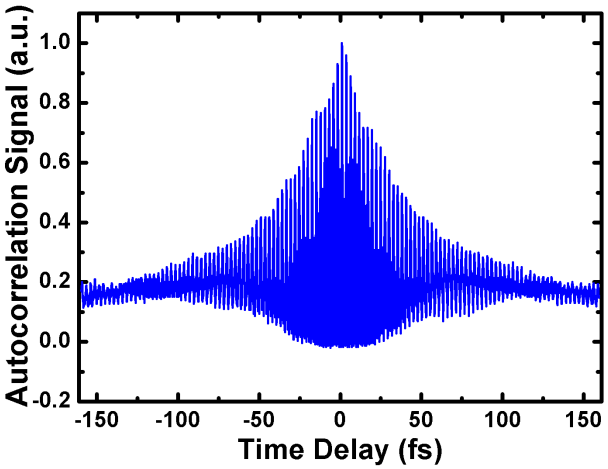

FIG. 4.20. Autocorrelation signal in order of 80 fs with $\gamma = 1$.

consecutive fringes in the autocorrelation measurement.

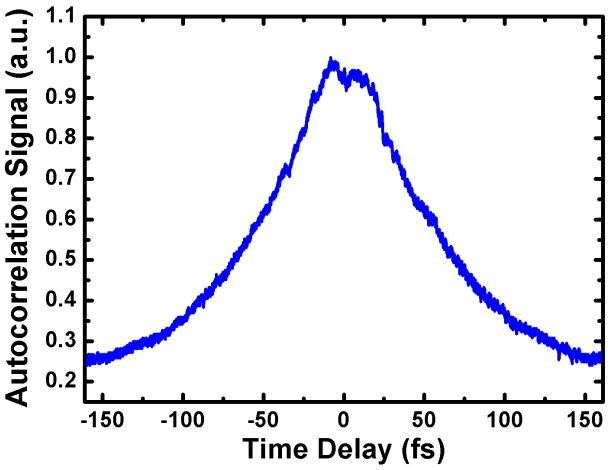

FIG. 4.21. Autocorrelation envelope with the $\gamma = 0$.

The measurements obtained from the experiment for the full-width-at-half-maximum and the pulse duration are 114 fs and 80 fs respectively.

All three autocorrelation techniques used in this study produced pulse lengths that are very similar. This shows how the pulse shaper autocorrelator can produce autocorrelation measurements which can be trusted. The big advantage of the pulse shaper autocorrelator is that it is possible to shape the pulse arbitrarily, make exact copies of the pulse and

perform an autocorrelation measurement on this shaped pulse all with the $4f$-shaper and in the exact position where the experiment is planned. In this way, the exact pulse shape of the pulse interacting with your experiment can be determined.

4.4.5 Transfer function results

In this section some example transfer functions were loaded onto the SLM in the $4f$-shaper and their influence on the output spectrum was measured. The spectrum was detected using an Avanetes Ava Spec-3648 spectrometer which, together with the SLM, was controlled by a computer.

4.4.5.1 Central transfer function

The transfer function used for this measurements is similar to the one used in the numerical simulation, given by Equation (4.3). The number of data points in this function corresponds to the number of pixels of the SLM, namely $n = 640$ (see Equation (4.4)).

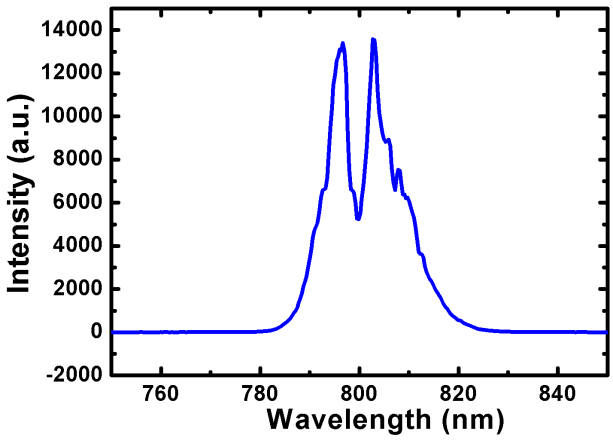

FIG. 4.22. Ouptut spectrum after the central frequencies were blocked.

The measurements where done by blocking a hundred components ($q = 100$) in the middle of the transfer function range and considering the amplitude while no attenuation was applied across the rest of the display. The output spectrum was measured and is shown in FIG. 4.22. The gap in the middle (around 800 nm) of the spectrum is clearly visible where

the spectral components were blocked.

4.4.5.2 Periodic transfer function

For this experiment, a periodic transfer function, similar to the one described in subsection 4.3.2, was displayed on the SLM. The transfer function consisted of alternating units of a hundred ones followed by a 100 zeros. FIG. 4.23 shows the output spectrum after the periodic transfer function has been applied. The periodic structure in the output spectrum is clearly visible.

The minima in the spectra observed in FIGs. 4.22 and 4.23 do not go down to zero, as might be expected compare to the simulations of the product $P(a.u)$ to the left in FIGs. 4.9 and 4.11. This is mainly due to the fact that the average of the measured intensity of the noisy signal is not zero and the alignment of the system can still be improved.

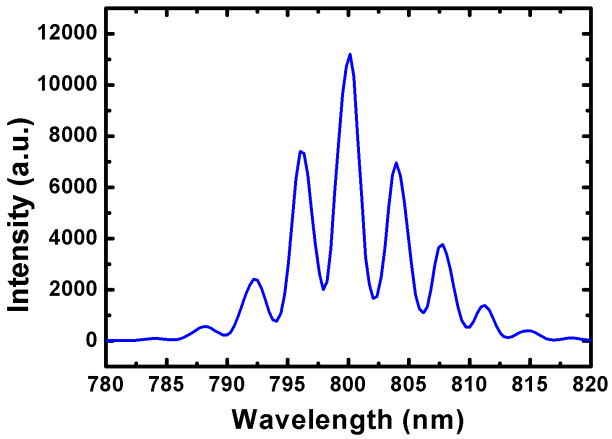

FIG. 4.23. Output spectrum after the application of a periodic transfer function.

Chapter 5

Conclusion

This work focused on spectral and temperal modulation of femtosecond laser pulses by using a liquid crystal spatial light modulator (LC-SLM) implemented in a $4f$-geometry. This was done by both modeling the $4f$-pulse shaper setup using Fourier optics as well as conducting experiments to characterize the ultra-short laser pulses.

Furthermore, experiments were conducted to show the versatility and power of the pulse shaping technique. To this end, the $4f$-pulse shaper was used to perform an autocorrelation measurement and this measurement was compared to traditional autocorrelation measurements.

The pulse length of the ultra-short pulses from a Ti:Sapphire femtosecond (fs) laser was measured using three different autocorrelation techniques. These were the intensity autocorrelation, interferometric autocorrelation and pulse shaping autocorrelation techniques. The setups used for these measurements were described and implemented. The assumed temporal pulse shape for these measurements was a Gaussian pulse.

The first technique, the intensity autocorrelation, gave a pulse width of 94 fs. The second technique, the interferometric autocorrelation, gave a pulse duration of 86 fs. Lastly the $4f$-pulse shaper was used to perform an autocorrelation measurement. This measurement gave a pulse duration of 80 fs. The measurement obtained from the interferometric autocorrelator compared well to that of the pulse shaping autocorrelator, where in both cases a peak to background ration of $8:1$ was obtained. This lends credibility to the measurement as it indicates near perfect alignment. Finally, instructive amplitude modulation was

employed in the $4f$-pulse shaper to illustrate its capabilities.

Bibliography

[1] *SLM-S640d and SLM-S320d Technical Documentation.*

[2] P. P. Banerjee. *Nonlinear Optics, theory, mumerical modeling and applications.* Marcel Dekker, 2004.

[3] T. Baumert, T. Brixner, M. Seyfried, and G. Gerber. Femtosecond pulse shaping by an evolutionary algorithm with feedback. *Applied Physics*, B65:779–782, 1997.

[4] R. W. Boyd. *Nonlinear Optics second edition.* Academic Press, 2003.

[5] R. W. Boyd. *Nonlinear optics third edition.* Konstantinos G, 2007.

[6] I. Bronstein. *Taschenbuch der Mathematik.* Feubuer, Leipzig, 1979.

[7] W. T. Cochran and J. W. Cooley. What is the fast fourier transform? *IEEE*, 55:10, 1967.

[8] M. Dekker. Laser and gaussian beam propagation and transformation. *Inc. All Rights Reserved*, 10016:999–1013, 2003.

[9] W. Demtröder. *Laser spectroscopy (third edition).* Springer-verlag, 1981.

[10] J. C. Diels and W. Rudolph. *Ultrashort Laser Pulse Phenomena.* Elsevier Inc, 2006.

[11] T. Feurer and G. Roberts. *Femtosecond Light: Optics and Interactions.* 2009.

[12] G. R. Fowles. *Introduction to modern optics.* Canada by General publishing company, 1975.

[13] C. Froehly, B. Colombeau, and M. Vampouille. Femtosecond pulse shaping using spatial light modulators. *Progress in Optics*, 20:65–153, 1983.

[14] E. Fruker and Y. Silberberg. Phase and ampliude pulse shaping with two-dimensional phase-only spatial light modulators. *J. Opt. Soc. Am*, B24:12, 2007.

[15] A. Galler and T. Feurer. Pulse shaper assisted short laser pulse characterization. *Applied Physics*, B 90:427–430, 2008.

[16] J. W. Goodman. *Introduction to Fourier Optics*. Roberts & Company publishers, 2005.

[17] D. Goswami. Optical pulse shaping approaches to coherent control. *Physics Reports*, 374:385–481, 2003.

[18] E. Hecht. *Optics*. Publishing as Addison Wesley, 2002.

[19] M. Hentschel, R. Kienberger, C. Spielmann, G. A. Reider, N. Milosevic, T. Brabec, P. Corkum, U. Heinzmann, M. Drescher, and F. Krausz. Attosecond metrology. *Nature*, 414:509–512, 2001.

[20] S. Huang. Femtosecond first-order autocorelation measurement based one-photon induced photocurrent in si schottky diodes. *Optics and Laser Technology*, 40:1051–1054, 2008.

[21] H. P. Langtangen. *Python Scripting for Computational Science, Second Edition*. Springer-Verlag, 2004.

[22] A. Marquez, C. Cazorla, M. J. Yzuel, and J. Campos. Characterization of the retardance of a wave plate to increase the robustness of amplitude-only and phase-only modulations of a liquid crystal display. *Modern Optics*, 52:4:633–650, 2005.

[23] B. J. Massman, R. Lausten, and A. Stolow. Focusing of light following a 4-f pulse shaper: Considerations for quantum control. *Physical Review*, 77:043416, 2008.

[24] C. Rulliere. *Femtosecond Laser Pulses*. Springer Science+Business Media, Inc, 2005.

[25] W. T. Silfvast. *Laser fundamental*. Cambridge University Press, 2004.

[26] R. Trebino. *Frequency-Resolved Optical Gating*. Kluwer Academic, 2000.

[27] S. Vaingast. *Beginning Python Visualization: Crafting Visual Transformation Scripts*. Springer-Verlay, 2009.

[28] F. Verluise, V. Laude, Z. Cheng, C. Spielmann, and P. Tournois. Amplitude and phase control of ultrashort pulses by use of an acousto-optic programmable dispersive filter: pulse compression and shaping. *Opt. Lett*, 25:575, 2000.

[29] A. M. Weiner. Femtosecond optical pulse shaping and processing. *Prog. Quant. Electr*, 19:161–237, 1995.

[30] A. M. Weiner. Femtosecond pulse shaping using spatial light modulators. *Review of Scientific Instruments*, 71:5, 2000.

[31] A. M. Weiner. Femtosecond laser pulses propagation in a uniaxial crystal. *Prog. Quant. Electr*, 19:161–237, 2003.

[32] P. Weis, O. Paul, C. Imhof, R. Beigang, and M. Rahm. Strongly birefringent metamaterials as negative index terahertz wave plates. *Appl. Phys. Lett*, 95, 2009.

[33] F. Weise, S. M. Weber, M. Plewicki, and A. Lindinger. Application of phase, amplitude, and polarization shaped pulses for optimal control on molecules. *Chemical Physics*, 332:313–317, 2007.